



MSc Physics and Astronomy

Advanced Matter and Energy
Physics

Master Thesis

Broadband light trapping patterns for ultrathin CIGSe and CZTS solar cells

by

M. Magdalena Solà Garcia
11017899

60 ECTS

June 2016 – June 2017

1st Examiner:

Prof. Dr. Albert Polman

Supervisors:

Verena Neder, MSc
Dr. Mark Knight

2nd Examiner:

Prof. Dr. Tom Gregorkiewicz

AMOLF

*Center for Nanophotonics, AMOLF
Science Park 104, 1098 XG
Amsterdam, The Netherlands*

ABSTRACT

Thin film solar cells offer a potential reduction in fabrication and material costs compared to conventional solar cell geometries, together with the possibility of flexible devices. Nevertheless, the reduced absorber thickness, usually below $1\ \mu\text{m}$, implies a decrease in the absorption of light and, therefore, a reduction of the efficiency. We address this absorption loss by studying the coupling of light incident on the solar cells into the optical waveguide modes supported by the absorber layer. In previous works this coupling was only shown either at specific wavelengths or in a very broad spectral range, with periodic and random arrays of nanoparticles, respectively. In contrast, in this thesis we focus on optimized arrays of nanoparticles and textures, *zebra* patterns, that allow for the excitation of waveguide modes in the desired range of wavelengths.

We fabricate periodic, random and optimized arrays of cylindrical nanoparticles with substrate conformal imprint lithography, while the zebra patterns are fabricated by means of two different techniques: focus ion beam (FIB) and electron-beam lithography. All structures are constituted of Si patterns on top of a Si substrate. We measure the power spectral density (PSD) of all patterns with a home-built Fourier microscope, which allows us to recover the angular distribution of the light scattered by the structures. The results show that the optimized array of nanoparticles and zebra pattern exhibit a distribution of the intensity of the diffracted light in the desired range of momenta, $k_{||}$, which can be tailored to match with the wavevectors of the waveguide modes. In particular, the zebra pattern shows a high concentration of diffracted light within the selected range of momenta, thus being more desirable for photovoltaic applications.

As a next step, we demonstrate the coupling of light into waveguide modes in thin film solar cells by periodic and optimized structures. First, we consider a $\text{CuIn}_x\text{Ga}_{1-x}\text{Se}_2$ (CIGSe) solar cell with a periodic pattern of SiO_2 nanoparticles on an indium tin oxide (ITO) substrate. We find that the measured external quantum efficiency (EQE) exhibits an overall improvement and, in particular, we can distinguish peaks at the wavelengths in which the momentum provided by the grating matches with the wavevectors of the modes. Secondly, we evaluate absorption enhancement of ultrathin $\text{Cu}_2\text{ZnSnS}_4$ (CZTS) solar cells containing the optimized zebra patterns, fabricated of SiO_2 on top of a molybdenum substrate, by performing finite-difference time-domain (FDTD) simulations. The results show an increase in absorption over broad ranges of wavelengths, leading to a predicted 6 % rise of the short current density with respect to the unpatterned cell.

Finally, we investigate the optical properties of CZTS solar cells through cathodoluminescence (CL) spectroscopy. We observe that our sample, which consists of a CZTS layer with a thin film of CdS on top, does not exhibit significant variations in the luminescence spectra over different regions, with separations up to a few millimetres. Main intensity peaks are observed at 520 and 920 nm, corresponding to emission from CdS and CZTS, respectively. An additional peak at 760 nm is observed, which is attributed to CdS or the CdS/CZTS interface.

Overall, this thesis provides insight into the scattering of light from nanostructured interfaces, which can lead to further light trapping enhancement in thin film solar cells.

TABLE OF CONTENTS

Abstract	3
Table of Contents	5
Chapter I: Introduction	7
1.1 Ultrathin solar cells	7
1.2 Light coupling into waveguide modes	7
1.3 Outline of the thesis	9
Chapter II: Fourier microscopy	11
2.1 Introduction to Fourier microscopy	11
2.2 Experimental setup	12
2.3 Characterization of the microscope	14
Chapter III: Fabrication and measurement of optimized nanopatterns	19
3.1 Arrays of nanopillars	19
3.2 Zebra patterns	23
3.3 Discussion and outlook	29
Chapter IV: Applications in solar cells	31
4.1 Periodic arrays for light trapping in CIGSe solar cells	31
4.2 Zebra patterns for light trapping in CZTS solar cells	33
4.3 Discussion and outlook	39
Chapter V: Cathodoluminescence spectroscopy on CZTS	41
5.1 Introduction to CL spectroscopy	41
5.2 Energy-dependence of the penetration depth of e^-	42
5.3 Large area integrated intensity map	43
5.4 CL spectra at different positions	44
5.5 CL spectroscopy at low temperature	48
Chapter VI: Conclusions and outlook	51
Bibliography	55
Acknowledgements	59
Chapter A: Additional characterization of Fourier microscope	61
A.1 Measurements at 490 nm	61
A.2 Dye experiment to obtain NA	63
Appendix B: Optical data	65
B.1 Optical data	65
Appendix C: Additional information of CL measurements	67
C.1 Comparison of different regions	67
C.2 Fitting of the CL spectra	68

Chapter 1

INTRODUCTION

1.1 Ultrathin solar cells

Solar cells have achieved a remarkable development in the last years, with record efficiencies up to 27.6 % for conventional single junction silicon cells [1] and decreasing price per generated watt [2, 3]. However, new challenges arise for photovoltaics (PV) to be able to fully compete with conventional energy sources, such as a further reduction of the cost per module, in addition to other features such as its integration into buildings and the landscape, among others. Thin film PV can address this reduction in cost by allowing a substantial decrease in the amount of material used and fabrication expense, since it allows a decrease in absorber thickness from the conventional 100-200 μm for Si solar cells to a few hundred nanometre for thin film PV materials. This reduction in thickness yields new opportunities in PV, such as the fabrication of flexible devices that can be combined with electronics, buildings or other objects. However, the use of thinner layers also implies a decrease in absorption of light and therefore research is needed to address this problem by cost-efficient light trapping strategies.

Light incident on a solar cell travels through the absorbing film, where part of it will be absorbed and the rest will be transmitted and, thus, lost, unless the cell contains an effective light management mechanism. We can characterize the loss in absorption due to a reduction in thickness by calculating the absorption length of a material, δ_p , which describes the distance that light needs to travel inside a material for its intensity to decrease by $1/e$ ($\delta_p = \lambda/4\pi\kappa(\lambda)$, where λ is the free space wavelength and κ is the imaginary part of the refractive index). Figure 1.1 shows the absorption length as a function of the wavelength for Si, GaAs, which holds the current record efficiency for single junction cells [1], and two thin film materials, $\text{Cu}_2\text{ZnSnS}_4$ (CZTS) and $\text{CuIn}_x\text{Ga}_{1-x}\text{Se}_2$ (CIGSe). From the figure we can already see that Si is not well suitable for thin film photovoltaics due to its small absorption length, thus research needs to be focused on alternative materials. Moreover, even if the absorption length is already low for GaAs, CIGSe and CZTS, reduction of thickness below 1 μm still demands for light trapping solutions.

1.2 Light coupling into waveguide modes

An approach to improve the absorption of light inside thin film (or ultrathin) solar cells is to study light coupling into waveguide modes. Most photovoltaic materials have a high refractive index and, thus, support waveguide modes, in which light can propagate in the longitudinal direction of the film. Hence, nanostructured patterns can be used to redirect light into these modes by adding an in-plane momentum $k_{||}$ to the incident light that matches with the wavevectors of the guided modes. In conventional thick solar cells, the absorber supports a large amount of modes, thus nanopatterns are used to redirect light towards angles higher than the critical angle. Nevertheless, when the thickness of the

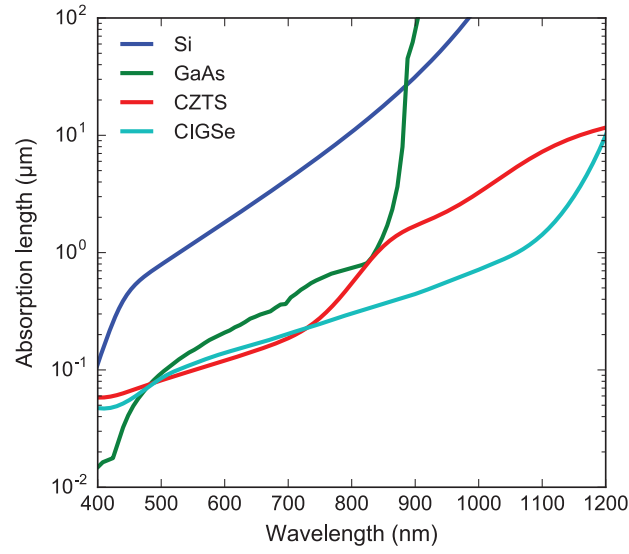


Figure 1.1: **Absorption length of Si, GaAs, CZTS and CIGSe as a function of the wavelength.** Optical data for Si and GaAs has been extracted from ref. [4], while the one from CZTS and CIGSe have been obtained from ellipsometry measurements [5] and are discussed in appendix B.

absorber is reduced down to a few hundreds of nm, only a set of discrete waveguide modes are supported and, therefore, further optimization is needed to match the momentum given by the nanopatterns with these modes.

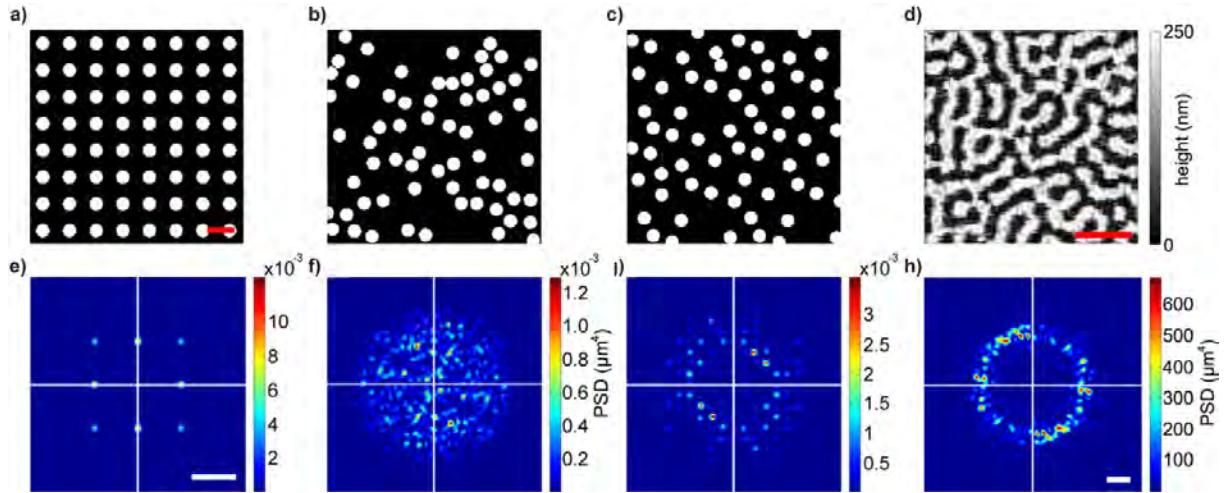


Figure 1.2: **Power spectral density (PSD) maps of different patterns of nanostructures, obtained from ref. [6].** (a-c) Real space maps of periodic (a), random (b) and optimized (c) arrays of nanocylinders, together with an optimized texture (d). The scale bar indicates 500 nm in all cases. (e-h) Corresponding 2D PSD spectra of the previous patterns. Here the scale bar indicates $13 \text{ rad } \mu\text{m}^{-1}$ and the horizontal and vertical axes correspond to k_x and k_y . The periodic pattern shows strong peaks at specific momenta, which is not optimum if we want broadband light trapping, while the random pattern provides a range of momenta that is too broad compared to the available modes. As an alternative, the optimized array of nanocylinders and the texture allow to tune the distribution of the peaks within a certain range of $k_{||}$.

A way of analysing the momentum provided by a pattern of nanostructures is through the 2D spatial Fourier transform, or power spectral density (PSD), of the pattern. The Fourier, or k -space, map gives information about the momentum provided to the light that is diffracted by a given pattern of nanostructures, and thus it is a useful tool to evaluate the potential coupling to waveguide modes. A common pattern used in photovoltaics is a periodic grating of nanostructures, such as nanocylinders, as shown in figure 1.2 (a). In this case, light is diffracted following the grating equation, and therefore the provided in-plane momentum can only take a set of discrete values of $k_{||}$, as can be seen from the Fourier transform of the pattern (fig. 1.2, b). Notice that here the horizontal and vertical axes correspond to k_x and k_y respectively, with $k_{||} = \sqrt{k_x^2 + k_y^2}$. The exact positions in k -space of the peaks of PSD are determined by the periodicity of the grating and correspond to the different diffraction orders. This momenta provided by the grating already allows for an enhancement in the absorption of solar cells due to coupling to waveguide modes, as shown in several works [7–9]. However, the $k_{||}$ given by a grating can only match the wavevectors of the waveguide modes at very specific wavelengths, according to the dispersion relation of the layer in consideration. In contrast to this, random patterns of nanostructures can scatter light to any direction due to the lack of periodicity. An example of a random pattern of nanocylinders is shown in figure 1.2 (b), together with its corresponding Fourier transform (f). In this case, all values of $k_{||}$ can be achieved up to a maximum, related to the minimum spacing between the nanocylinders. Nevertheless, the range of $k_{||}$ given by these patterns is too broad compared to the range of wavevectors available to couple to, as will be described further on.

Van Lare *et al.*[6] demonstrated a method for optimizing a pattern of nanocylinders via a Monte Carlo algorithm in order to maximize its corresponding PSD within a certain range of $k_{||}$. The particular value of this range depends on the dispersion relation of the film. The real and Fourier space of this optimized pattern is shown in figure 1.2 (c and i, respectively). We can observe that even if the real space looks random, the peaks in the k -space are concentrated inside a ring within a certain range of $k_{||}$. As a further optimization, it was also shown that a texture as the one shown in figure 1.2 (d) instead of a pattern of nanocylinders allowed for a better enhancement of the PSD in the desired range of momenta. In this case (fig. 1.2, h) the PSD is highly concentrated inside the ring in k -space, and becomes practically zero outside of this area. From here on we will refer to this optimized texture as a *zebra* pattern.

1.3 Outline of the thesis

This thesis aims to evaluate experimentally the scattering of light by the patterns proposed by van Lare *et al.* and to study their performance when integrated in particular solar cells. In **Chapter 2**, we discuss the Fourier microscopy setup that was built to study the diffraction of light by nanopatterns. Subsequently, in **Chapter 3** we present the fabrication of the patterns and the measurements of their PSD in the Fourier microscope. **Chapter 4** then evaluates the approach of light coupling into waveguide modes through two different examples: a CIGSe solar cell, for which absorption enhancement with a periodic nanopatterning has already been tested, and a CZTS cell, for which simulations have been done

to prove the effectiveness of the zebra patterns. Finally, we also investigate the optical properties of current CZTS solar cells by studying the material, provided by Jeana Hao's group from University of New South Wales (UNSW Sydney), with cathodoluminescence spectroscopy. This method allows us to evaluate the luminescent properties of the materials and possible band gap variations with respect to the expected ones over different positions and depths.

Chapter 2

FOURIER MICROSCOPY

In order to experimentally verify the behaviour of the optimized patterns we need a setup that can measure the direction of the scattered light or, equivalently, the Fourier transform of the structures. This was done by means of a home-built Fourier microscope, which is described in this chapter.

2.1 Introduction to Fourier microscopy

Fourier microscopy allows to recover the direction in which light is radiated from an object. The simplest Fourier system is a lens: when an object placed at the front focal distance of a lens is illuminated, the 2D-transform of the emitted field is reproduced at the back focal plane (BFP). In other words, each direction of the emitted light that can be captured by the lens corresponds to a single point in the back focal plane. In order to retain the largest possible angles we can use an objective instead of a lens.

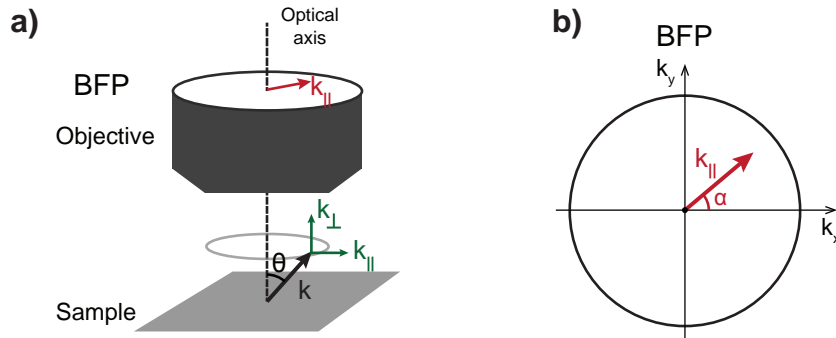


Figure 2.1: Schematic of the relation between the emitted light and the back focal plane of the objective. (a) For each different angle θ of the emitted light the parallel component of the wavevector, $k_{||}$, corresponds to a point at the BFP of the objective. Therefore, the BFP can be identified as a circle in the k -space, with its radius given by the numerical aperture (NA) of the objective. (b) Geometry of the BFP, with each point being determined by a radius $k_{||} = \sqrt{k_x^2 + k_y^2}$ and angle $\alpha = \tan(k_y/k_x)$.

Figure 2.1 (a) depicts the relation between the emitted light and the BFP of the objective. The coordinates at the BFP correspond to the parallel momentum, $k_{||}$, of the light, which can be described as:

$$k_{||} = k_0 n_m \sin \theta \quad (2.1)$$

where n_m is the refractive index of the propagating medium, k_0 is the wavenumber in free space, related to the free space wavelength λ_0 by $k_0 = 2\pi/\lambda_0$, and θ is the angle of the outgoing light with respect to the optical axis. Therefore, the BFP is a circle in the k -space, as shown in fig. 2.1, with its radius determined by the maximum angle that can

be captured by the objective, i.e., its numerical aperture (NA), defined as:

$$\text{NA} = n_m \sin \theta \quad (2.2)$$

Due to the geometry of the objective the BFP is contained inside it, thus we need additional optical components to reproduce it.

2.2 Experimental setup

A schematic of our home-built setup for Fourier imaging is shown in figure 2.2. The setup is built to measure only in reflection, meaning that the objective is used both to send light on the sample and to capture the scattered light. Therefore, we can divide the setup into two main parts: the illumination of the sample and the collection of the scattered light and subsequent formation of the real and Fourier images. In addition to this, since we use immersion oil to achieve a high NA, it is preferable to have the sample placed horizontally on a moving stage. Hence, we need a simple periscope before the objective to change the optical axis from horizontal to vertical.

2.2.1 Illumination of the sample

In our setup we have two illumination sources. The first one is an LED, which is mainly used as a help for focusing on the sample when starting an experiment. The main source in our experiments is a supercontinuum laser (ExtremeK, Fianium), which provides nearly unpolarized collimated white light in the spectral range 350-1750 nm. After this, we can use a filter (LLTF contrast, Fianium) to select the desired wavelength. The wavelength used for the experiments was 405 nm, which allows us to obtain a range of momentum k that is large enough, as shown in eq. 2.1, and at the same time this wavelength is still inside the operating range of most optical components. In addition to the measurements at 405 nm, we also performed them at 490 nm to test the performance of the microscope at different wavelengths. The results at this wavelength are shown in appendix A.1.

Since our setup works in reflection, the light from the source goes through a high-NA 100x objective (Nikon, WD=0.13 mm, NA=1.4 oil immersion). However, instead of using the objective to focus the light on the sample, as usually done, we want to have a collimated beam with normal incidence on the sample. This can be achieved by placing a lens between the laser and the objective. The distance between the lens and the BFP of the objective needs to be exactly the focal length of the latter, f_F , which in our case was 30 cm. In this way, the collimated beam coming from the laser is focused on the centre of the BFP of the objective, which corresponds to an angle of zero degrees with respect to the objective axis. The spot size on the sample is around 20 μm , which can be measured by using a mirror as a sample.

2.2.2 Real and Fourier space imaging

We have two imaging modes: real and Fourier space. The change between both can be done by flipping in or out the corresponding optical components (in green in fig. 2.2). The real space mode works as in conventional microscopes: the light is collected by the objective to form an image. Since our objective is infinity corrected, we need a tube lens

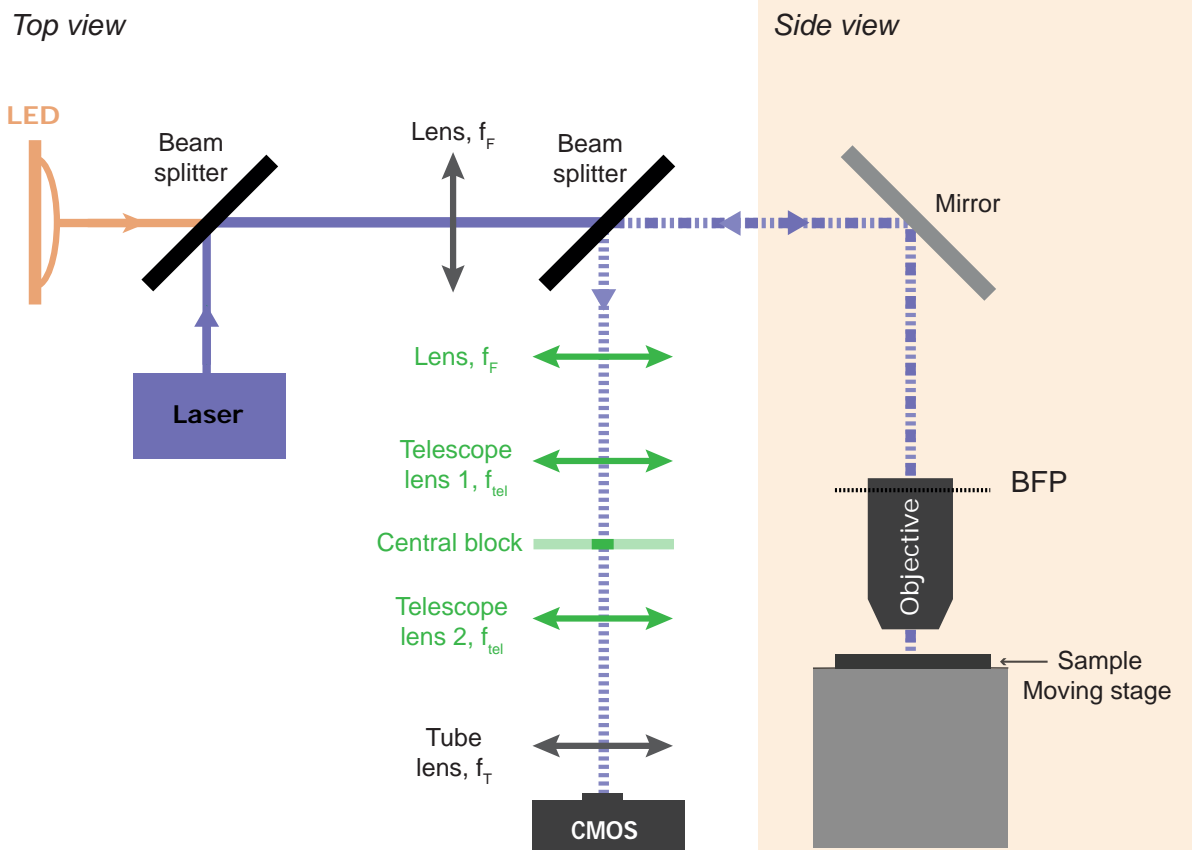


Figure 2.2: **Schematic of the Fourier microscopy setup.** The microscope can be used for real and Fourier space imaging. The components in green are only needed for Fourier-space imaging. In this case, the beam from the laser is focused with a lens ($f_F = 30$ cm) on the back focal plane (BFP) of the objective. The light is incident on the sample with normal incidence and the scattered light is collected by the objective. The BFP can be imaged through a Fourier lens ($f_F = 30$ cm). The BFP is first reproduced using a telescope ($f_{tel} = 10$ cm) to block the centre (corresponding to low momentum k) and after that is reproduced again with a tube lens ($f_T = 20$ cm) on a CMOS sensor. For real space imaging, only this last lens is needed.

($f_T = 20$ cm) to focus the light on a CMOS sensor (DCC1645C, Thorlabs), which allows us to obtain the image. The distance between the objective and the tube lens is arbitrary, while the distance between the latter and the CMOS sensor is f_T .

The Fourier space mode demands for an extra lens located at a distance equal to its focal length, $f_F = 30$ cm, with respect to the BFP of the objective. This would be enough to image the BFP on the CMOS. However, when imaging the Fourier plane, the intensity on the centre, corresponding to low spatial frequencies, is very high. This is due to the strong 0-order diffraction and reflections from the objective produced when focusing the laser beam on the BFP. In order to avoid saturation of the CMOS sensor, we filtered the centre by reproducing the Fourier plane through a telescope, with $f_{tel} = 10$ cm, and physically blocking the centre. The block consisted of a 250 nm-thick spot of chromium, with a diameter of 200 μm , sputter coated on a 170 μm -thick glass slide.

2.3 Characterization of the microscope

Three main characterization and calibration experiments have been developed in order to test the functioning of the microscope and include any necessary corrections.

2.3.1 Numerical aperture

The first experiment is to characterize the experimental NA of our Fourier microscope, which should be around 1.4 as given by the manufacturer, and to obtain a relation between the size of the image on the CMOS sensor (in pixels) and the corresponding $k_{||}$. We performed a test with a fluorescent dye (absorbing at wavelength $\lambda_{abs} \simeq 405$ nm and emitting at $\lambda_{em} \simeq 650$ nm) on a glass slide. The main idea is that light emitted by the dye with $k_{||} < k_0$ can easily escape to the air below the sample, while the rest of the light with $k_{||}$ up to $NA\ k_0$ will be captured by the objective. Details about this experiment are explained in appendix A.2.

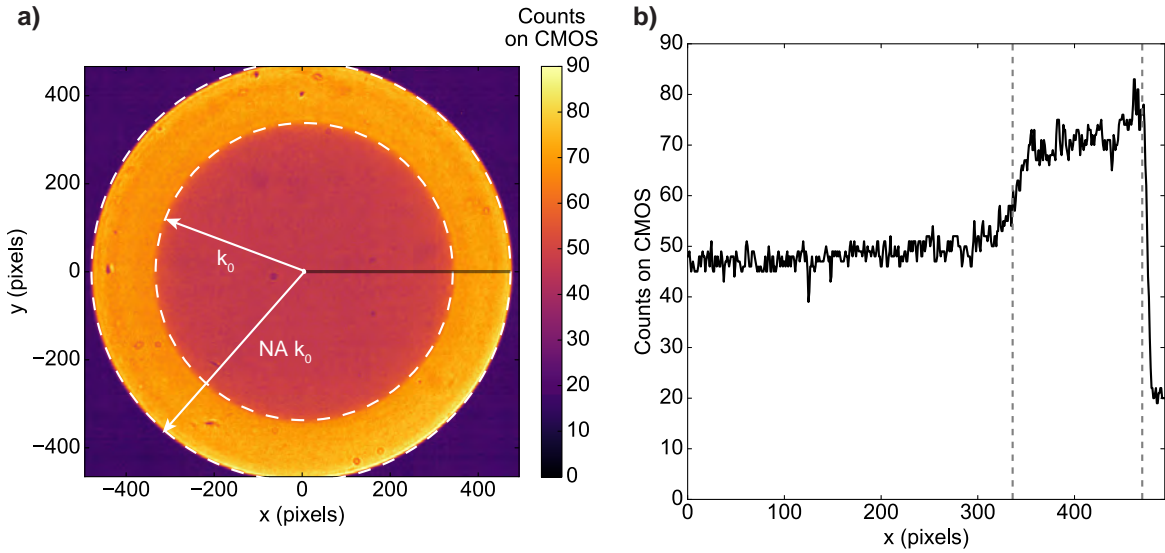


Figure 2.3: Emission of a fluorescent dye. (a) The Fourier image depicts the intensity of the light emitted by the dye as a function of the position on the CMOS sensor. The highest intensity circle corresponds to the BFP, while the circle with lower intensity matches the escape cone of light emitted by the dye. (b) Cross-section corresponding to the black line in (a). The two dotted lines indicate the main changes in intensity, matching the position in pixels of the circles in (a).

Figure 2.3(a) shows the k -space image obtained with our Fourier microscope. The horizontal and vertical axes correspond to the x and y pixels of the CMOS sensor, while the colour indicates the number of counts, equivalent to the intensity of light incident on the sensor. The back focal plane can be identified in any Fourier image as a circle with high intensity compared to its outside. Hence, only the features contained inside the BFP hold information regarding the k -space, while the outside corresponds to background light, coming mainly from other sources of light in the room and noise from the CMOS sensor. In the example of the dye, the BFP can be easily identified as the area with the highest intensity, and we know that the radius corresponds to the maximum $k_{||}$ achievable, $k_{||\text{max}} = NA\ k_0$. Therefore, from this we can obtain the relation between $k_{||}$ and the pixels

on the CMOS. To better quantify it, figure 2.3(b) shows a cross-section corresponding to the line in black in fig. 2.3(a). In the figure we can see a sharp decay of the intensity at around $x = 470$ px, indicating the size of the BFP.

In this particular example of the dye we can see that in the BFP there is a second circle with a lower intensity, corresponding to the escape cone of the light, with $k_{||} < k_0$. This transition can be observed in fig. 2.3(b), between $x = 314$ px and $x = 356$ px. We can take an average of these two positions and obtain the ratio between the radius of the BFP and the one from the escape cone, which corresponds to the NA:

$$\text{NA} = \frac{\text{NA } k_0}{k_0} \simeq \frac{470 \text{ px}}{336 \text{ px}} \simeq 1.4 \quad (2.3)$$

Hence, the experimental NA matches with the one given by the manufacturer. Moreover, now we can obtain the value of $k_{||}$ represented by each pixel, k_{px} :

$$k_{px} = \frac{\text{NA } k_0}{470 \text{ px}} = 0.047 \text{ rad } \mu\text{m}^{-1} \text{ px}^{-1} \quad (2.4)$$

Notice that this value will depend on the wavelength of the source. Here we have used $\lambda = 405$ nm.

2.3.2 Distribution of $k_{||}$

Another important characterization of our Fourier microscope is the distribution of $k_{||}$ in the Fourier images. We expect $k_{||}$ to be linearly distributed on the BFP of the objective, thus our images should present the same arrangement. In order to test it, we used a $4 \mu\text{m}$ -pitch grating of Cr nanowires on top of inverted Si pyramids, provided by Mark W. Knight. Figure 2.4 (a) shows an SEM image of this grating, together with its Fourier image in fig. 2.4 (b). Despite the complexity of this sample, the main features that we observe in the Fourier image are the diffraction orders of the Cr grating, with $k_{||}$ given by:

$$k_{||} = \frac{2\pi}{\Lambda} \sqrt{m^2 + n^2} = 1.57 \sqrt{m^2 + n^2} \quad [\text{rad}/\mu\text{m}] \quad (2.5)$$

where Λ is the pitch ($4 \mu\text{m}$) and $m, n = 0, \pm 1, \pm 2 \dots$ refer to the different orders. This becomes particularly noticeable in the horizontal and vertical axes. Fig. 2.4 (c) and (d) show the cross-sections in these directions, in which we can observe that the distance between consecutive orders is held constant and equal to approximately $\Delta k = 1.49 \text{ rad } \mu\text{m}^{-1}$. This value is very close to the one expected for this grating (eq. 2.5), with the small discrepancy probably coming from errors in the exact determination of the positions of the peaks and of k_{px} .

As a final remark, we should notice that in the Fourier image the zero and lowest orders are blocked with the central block, as explained in section 2.2. This is done in order to avoid saturation of the image and will be a common feature in all of the Fourier images presented in this thesis.

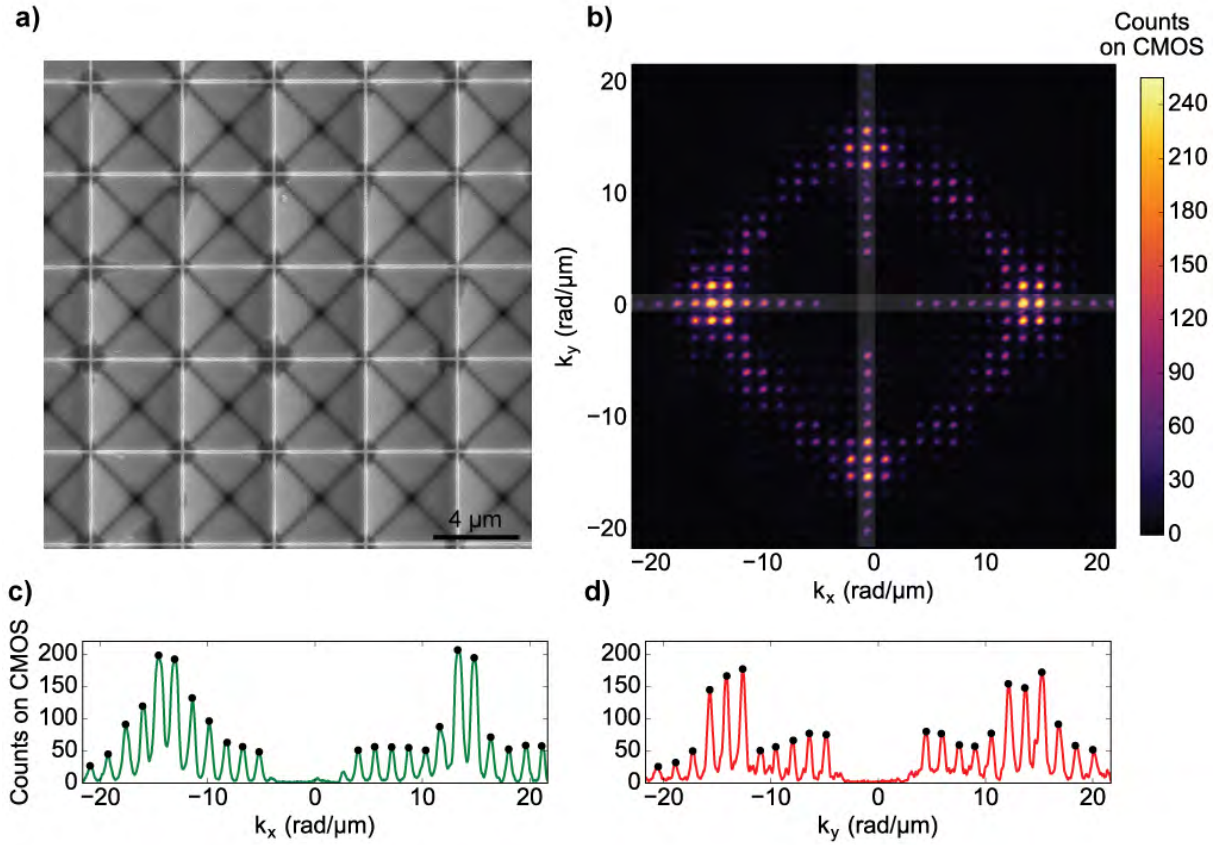


Figure 2.4: **Fourier imaging of a periodic grating.** (a) SEM image of a grating of Cr nanowires on top of inverted Si pyramids (made by Mark W. Knight), with its corresponding Fourier image (b). The grating behaviour is mainly exhibited in the indicated horizontal and vertical lines, in which each dot represent a diffraction order. Plots (c) and (d) show the cross-sections corresponding to these lines. The average spacing between the orders (maxima in the plots) is $2\pi/\Lambda$, with the periodicity Λ being $4\mu\text{m}$.

2.3.3 Intensity correction function

Finally, we need to characterize the intensity that we obtain in the Fourier images. Ideally we would expect that the value of intensity at each $k_{||}$ in our images matches the amount of light scattered by the sample with that momentum. However, in the experiments we need to take into account other factors that might affect this relation, such as angular dependence of the transmission of the objective, inhomogeneous illumination and vignetting, among others. Hence, we need to obtain a correction function that accounts for any of these effects by calibrating our setup with a sample that has a well-known distribution of the scattered intensity. Since in our experiments light arrives on the sample with only one angle (normal incidence), we need a sample that scatters light in all directions. We chose a commercial reflectance standard (Spectralon, Labsphere) that has a lambertian behaviour, i.e., the scattered intensity at each angle is given by:

$$I_{Lamb}(\theta) = I_0 \cos \theta \quad (2.6)$$

where θ is the angle with respect to normal to the sample, and I_0 is the intensity scattered at $\theta = 0^\circ$. This lambertian scattering is usually optimized for large fields of views, of the order of millimetres, since the particles that compose the material have sizes of the order of $100\mu\text{m}$. In contrast to this, the spot size of the light on the sample is around $20\mu\text{m}$ in our setup. In order to overcome this limitation, we took 50 measurements at different positions and averaged them, thus in this way we expect to retrieve the lambertian behaviour. In addition to this, since we are looking at the k -space, which has a non-linear distribution with respect to the angle θ , we need to convert eq. 2.6 into $k_{||}$ coordinates, which can be done by dividing by $\cos \theta$ [10]. Therefore, we would expect the intensity to be a constant:

$$I_{Lamb}(k_{||}) = I_0 \quad (2.7)$$

Hence, the correction function will be:

$$C(k_{||}) = \frac{I_{Lamb, CMOS}(k_{||})}{I_{Lamb}(k_{||})} = \frac{I_{Lamb, CMOS}(k_{||})}{I_0} \quad (2.8)$$

where $I_{Lamb, CMOS}$ is the intensity recorded by the CMOS at each $k_{||}$. In our case we do not have access to I_0 because we have the central block, but since we are only interested in the relative intensity among different $k_{||}$ we do not need to quantify it.

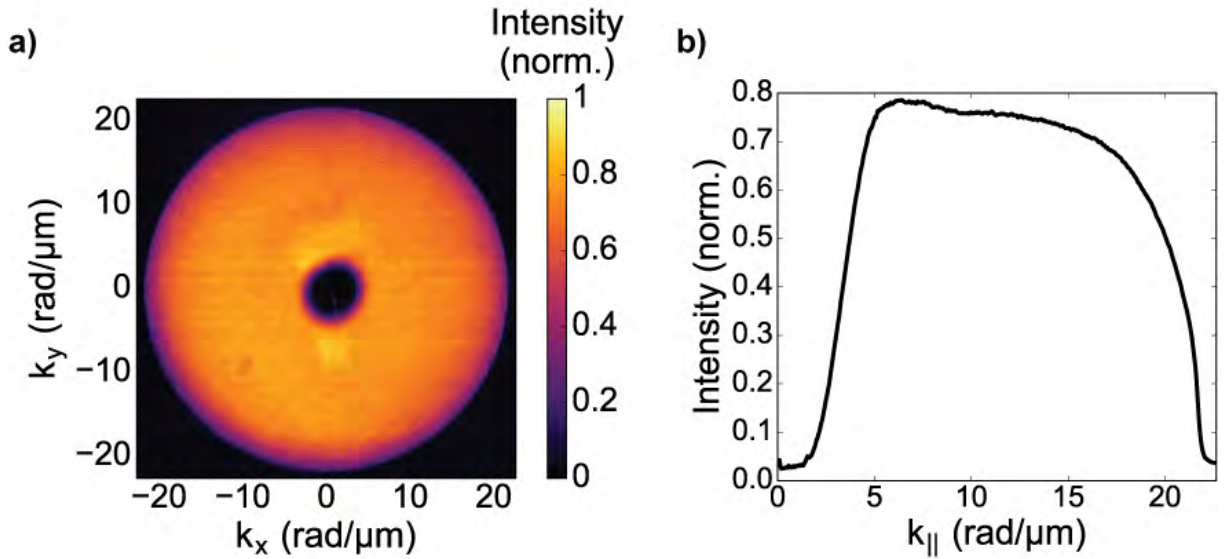


Figure 2.5: **Correction function of the intensity as a function of $k_{||}$.** (a) Fourier image of a Lambertian scatterer, obtained by averaging over 50 different positions on the sample. This image corresponds to the intensity correction function. (b) Plot of the intensity integrated over the polar angle. We cannot retrieve the intensity scattered at low momenta due to the presence of the central block. For intermediate $k_{||}$ the correction is more or less constant and decreases rapidly for momentum larger than $\sim 19 \text{ rad } \mu\text{m}^{-1}$ due to the apodization function of the objective.

The correction function $C(k_{||})$ obtained using eq. 2.8 is shown in figure 2.5 (a), in which the colour scale represents the normalized intensity (in arbitrary units). Moreover, we can integrate the image over the polar angle (indicated in fig. 2.1, b) to obtain the average value

as a function of the radius, in this case corresponding to $k_{||}$, as plotted in fig. 2.5 (b). We cannot obtain the intensity at low $k_{||}$ due to the presence of the central block, but becomes high for the first accessible values of $k_{||}$. From here on, the correction function decreases slowly with increasing $k_{||}$ up to $\sim 19 \text{ rad } \mu\text{m}^{-1}$, from where it decreases very rapidly, due to the apodization function of the objective and the entire setup [10, 11]. Finally, the correction function drops to zero as it approaches to $k_{\text{max}} = \text{NA } k_0$. Taking this correction function into account, the intensity in the Fourier image for any sample will be corrected such that:

$$I_{\text{real}}(k_{||}) = \frac{I_{\text{CMOS}}(k_{||})}{C(k_{||})} \quad (2.9)$$

where we call $I_{\text{real}}(k_{||})$ to the actual intensity that we would expect to be scattered by the sample.

Chapter 3

FABRICATION AND MEASUREMENT OF OPTIMIZED NANOPATTERNS

In this chapter we measure the power spectral density of the light trapping patterns designed by Claire van Lare in ref. [6]. This includes the fabrication of periodic, random and optimized arrays of nanopillars and of the optimized textures. In all cases, the Fourier transform of the fabricated structures can be performed and compared to the actual results from the Fourier microscopy measurements.

3.1 Arrays of nanopillars

We first focus on the three different arrays of nanopillars shown in fig. 1.2. The material chosen to fabricate these samples was Si, due to its high reflectivity, meaning that we will receive more signal in the Fourier microscope measurements, and ease of nanofabrication. Given that the diffraction of light is determined by the geometry of the sample rather than the material, we expect that the results observed in Si can be equally applied to other materials.

3.1.1 Fabrication

The arrays of nanopillars were fabricated using substrate conformal imprint lithography (SCIL) [12], in which a PDMS stamp containing the desired pattern is used to transfer it on a layer of silica sol-gel, which has been previously spin-coated on the Si wafer (1000 rpm for 30 s). This results in an array of sol-gel nanoparticles on top of the wafer with a thin residual layer of sol-gel in between them, which can be removed with a breakthrough etch. The remaining sol-gel nanoparticles can be used as a mask in the successive reactive ion etching (RIE) process, which allows for the directional etch of Si to obtain vertical structures with the desired height. Finally, the residual sol-gel can be removed with a 1% hydrofluoric acid (HF) solution. Figure 3.1 (a) shows a schematic of the fabrication steps and the parameters for the plasma etching are shown in table 3.1. In this particular case, we used a SCIL stamp containing a set of $2.5 \times 2.5 \text{ cm}^2$ fields of periodic, random and optimized arrays, all of them with approximately the same density of nanopillars. The random and optimized fields were designed by stitching together many of the $4 \mu\text{m}$ -sized arrays shown in fig. 1.2 (a-c).

Figure 3.1 (b) shows a scanning electron microscope (SEM) image of a cross section of the final nanopillars, which was made using a focused ion beam (FIB) with prior deposition of a layer of Pt to increase the contrast. From the cross section we can see that the height of the pillars is around 165 nm, as we already expected according to the etching time used. Moreover, the walls are not completely straight but tilted, thus forming a structure close to a truncated cone, with the top diameter of 125 nm and bottom one of 205 nm. This is a common effect in nanofabrication and could be improved by optimizing the spin-coating and RIE processes, but we do not expect it to have significant consequences for our purpose.

Parameters	Breakthrough etch	Si etch
Gases	Ar: 25 sccm CHF ₃ : 25 sccm	HBr: 48 sccm O ₂ : 2 sccm
Pressure	15 mTorr	7 mTorr
HF: Forward power	67 W	30 W
ICP: Forward power	0 W	750 W
Temperature	20 °C	50 °C
Etch rate	~ 15 nm/min	~ 155 nm/min

Table 3.1: Parameters of plasma etching (RIE) for breakthrough etch (sol-gel etch) and Si etch.

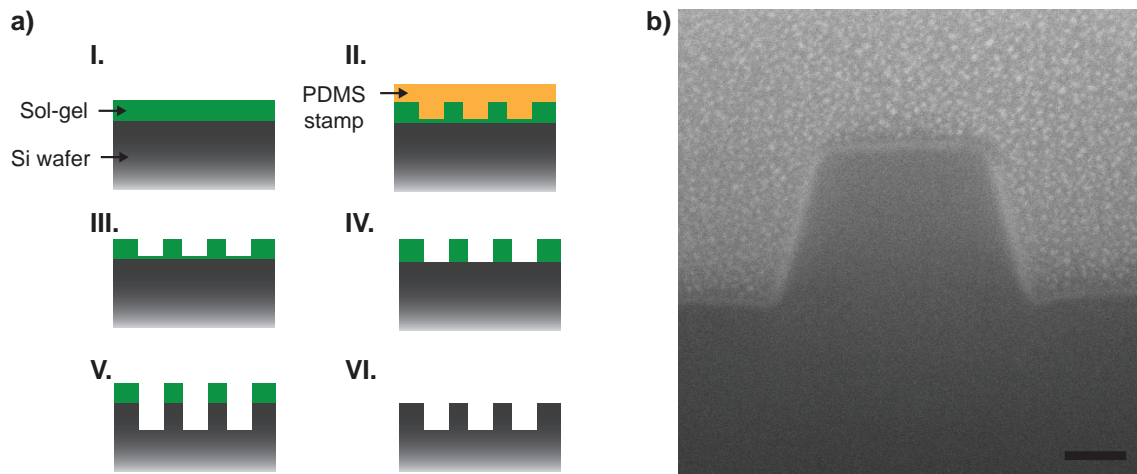


Figure 3.1: **Fabrication of array of Si nanopillars by SCIL.** (a) Schematic of the main steps in the nanofabrication procedure: a thin film (~ 70 nm) of silica sol-gel is spin-coated on a Si wafer (I) and a PDMS stamp is used to transfer a given pattern to this sol-gel film (II-III). After this, a breakthrough etch (RIE, Ar+CHF₃) is performed to remove the residual layer of sol-gel between the pillars (IV), and finally the thick sol-gel forming the pillars is used as a mask to etch the Si (RIE, HBr+O₂) (V). The remaining sol-gel is removed with an HF dip (VI). (b) SEM image of a cross section a Si nanopillar made with FIB. The scale bar indicates 50 nm. The height is approximately 165 nm and the top and bottom diameter are 205 nm and 125 nm, respectively. The grains on top of the pillar correspond to the deposited Pt.

An overview of the three types of arrays can be seen in fig. 3.2, with SEM images under an angle of 52°. The periodic array (a) clearly shows an ordered distribution of particles, with a pitch of around 400 nm. In contrast, both the random and optimized arrays (b and c, respectively) show a disordered distribution, without any observable periodic feature. In addition to this, we can observe that there are several small nanoparticles close to the main ones, which is probably due to defects present in the PDMS stamp. However, we do not expect these imperfections to have a significant effect in the PSD measurements.

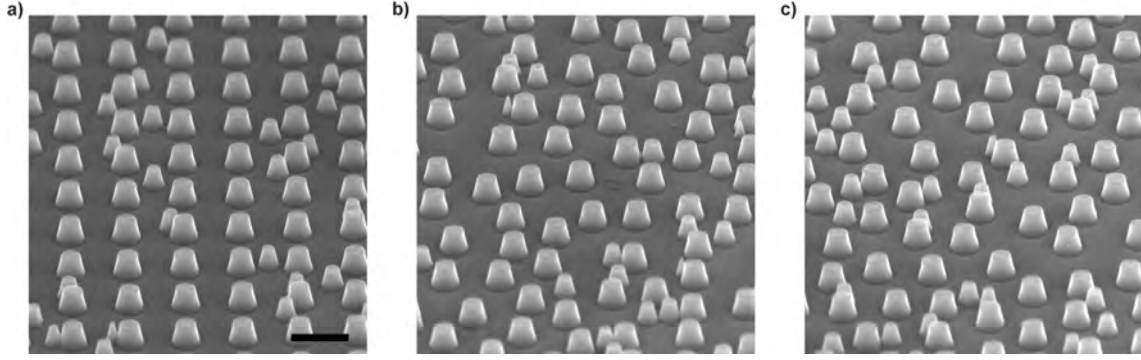


Figure 3.2: **SEM images of different arrays of nanoparticles fabricated with SCIL.** (a) Periodic, (b) random and (c) optimized arrays of nanoparticles, seen under an angle of 52° . The scale bar indicates 400 nm. In addition to the main nanoparticles, there are some smaller ones, which are defects from the fabrication.

3.1.2 Discrete 2D Fourier transforms

As a first approach to evaluate the power spectral density of the fabricated arrays, we can perform the two-dimensional discrete Fourier transform of the SEM images by using a fast Fourier transform algorithm [13]. We used top-view images with a total size of around $20\text{ }\mu\text{m}$, which is close to the field of view of our Fourier microscope, as discussed in section 2.2.1. The images and their corresponding 2D discrete Fourier transforms are shown in fig. 3.3 (a-c and d-f, respectively). The intensity in the maps has been normalized and the dashed white circle indicates the range of k that can be collected with our Fourier microscope. The zero-frequency component, which has a very high intensity indicating the average brightness of the image, has been removed for better visualization. In the experiments, this component would correspond to the light reflected by the arrays and depends on the reflectivity of the material and height of the structures [14].

The Fourier transform of an array of particles is composed of two main contributions: the shape of the particles, usually referred to as structure or form factor [15], and their distribution [16]. In our case, the form factor of a circular scatterer is an Airy pattern, with the Airy disk corresponding to a brighter circular region, as indicated by the arrow in fig. 3.3 (e), with size determined by the diameter of the particles. The main effect, however, comes from the distribution of the particles in each array. In the periodic structure (3.3, d), we can observe intensity peaks placed at the position $k_{||}=15.6\text{ rad }\mu\text{m}^{-1}$, corresponding to the first diffraction order of a grating as described in eq. 2.5, with periodicity $\Lambda=400\text{ nm}$. Here the intensity of the peaks is very high compared to the form factor, which is not visible in the map. In contrast, the Fourier transform of the random array shows a more distributed intensity over the entire Airy disk. In particular, there is a higher concentration in the range of momentum $11\text{--}23\text{ rad }\mu\text{m}^{-1}$, probably due to the fact that the array is not completely random but there is an average spacing among particles, ranging from 270 to 570 nm. Finally, the optimized array shows a similar Fourier pattern, but with the intensity distributed in a smaller range of momenta ($14\text{--}20\text{ rad }\mu\text{m}^{-1}$), as expected according to the optimization procedure.

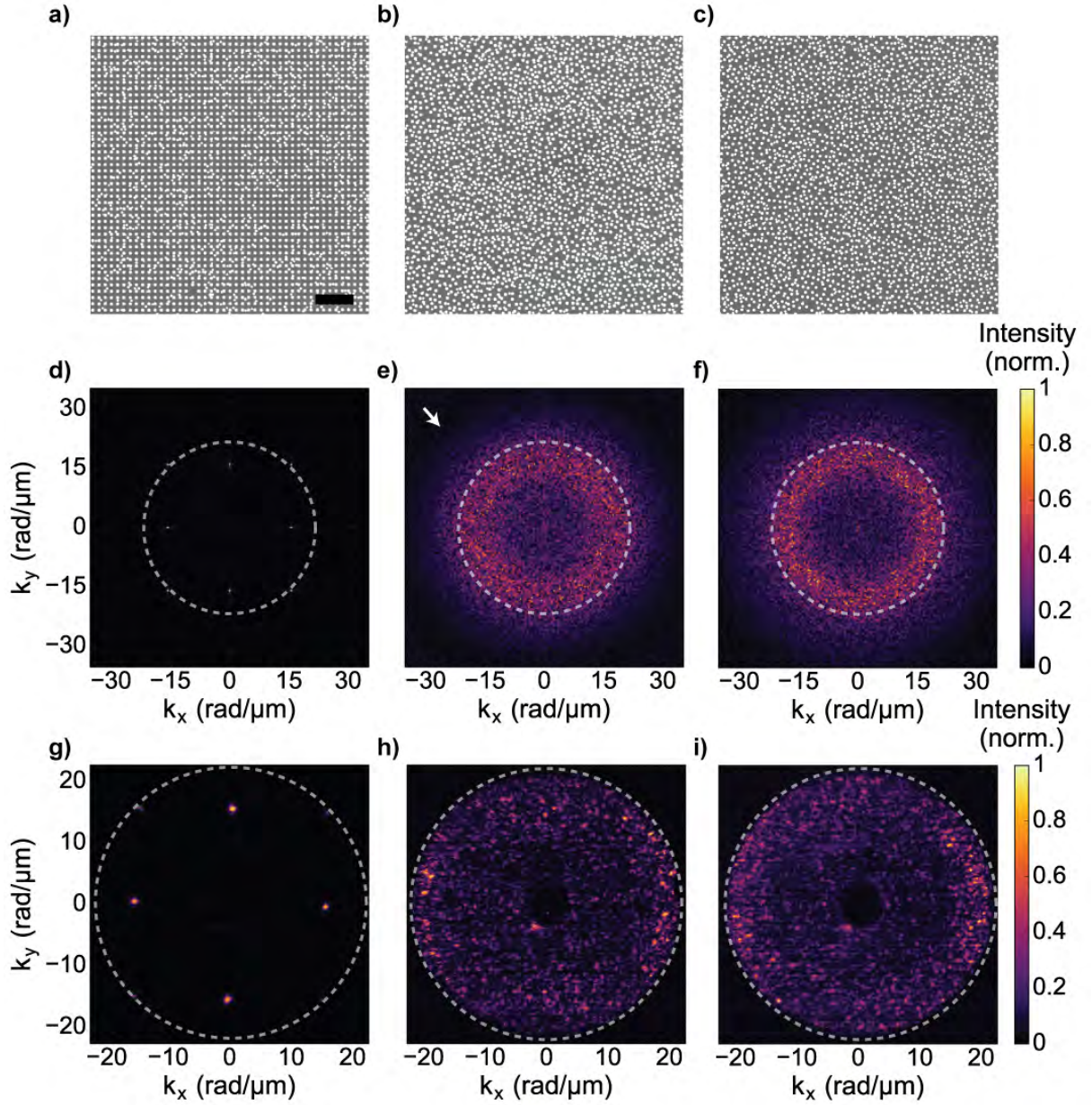


Figure 3.3: **SEM images of the arrays of nanoparticles seen from the top and their corresponding discrete 2D Fourier transform and Fourier microscopy images.** (a-c) Top view SEM images of the periodic, random and optimized arrays, respectively. The scale bar indicates 2 μm . (d-f) 2D discrete Fourier transforms of the SEM images. The white dashed line defines the maximum range of $k_{||}$ that can be obtained with our Fourier microscope, and the array in (e) indicates the Airy disk due to the circular shape of the particles. The Fourier transform of the periodic array (d) matches with the one from a periodic grating, with periodicity $\Lambda=400$ nm. The random array (e) shows a broad distribution of intensity, with a higher concentration at the $k_{||}$ corresponding to the average distances between particles, while the optimized array (f) exhibits high intensity in a narrower range of momenta. The corresponding diffraction patterns obtained with the Fourier microscope (g-i) show similar trends.

3.1.3 Measurements with Fourier microscope

The power spectral density of the nanoparticle arrays was measured using the Fourier microscope described in chapter 2. The intensity of the incident light was kept constant for

all the measurements, such that we can compare the scattered intensity between different samples. The obtained PSD maps are shown in figure 3.3 (g-i), in which the intensity is normalized with respect to the maximum for each image, and the dashed white circle indicates again the maximum $k_{||}$ achievable with the setup. For the periodic array (fig. 3.3, g), the Fourier image matches perfectly with the discrete 2D Fourier transform, with four peaks corresponding to the first diffraction orders ([0,1], [0,-1], [1,0] and [-1,0]). Moreover, in this case we can also see some contribution from the [11] orders, which are at the limits of the achievable values of $k_{||}$. In order to see clearly the intensity contribution at each $k_{||}$, figure 3.4 shows the integration of the images over the polar angle (α as depicted in fig. 2.1, b). For the periodic structure (blue curve) we can see again a high intensity peak at the expected value of $k_{||}$.

If we now look at the Fourier image of the random array (fig. 3.3, h), we can observe that the intensity of the diffracted light is distributed over the entire back focal plane, which was already expected from the discrete 2D Fourier transform due to the form factor, as discussed in 3.1.2. Nevertheless, this distribution is not homogeneous but the intensity becomes slightly higher for increasing $k_{||}$, which can also be observed in the plot of the integrated intensity (fig. 3.4, green line) and matches with the behaviour seen in the discrete 2D Fourier transform. Similarly, the Fourier image of the optimized array (3.3, i) also shows light distributed over the entire BFP. However, in this case we can distinguish more clearly a ring in the range of $k_{||}$ from 15 to 21 $\text{rad } \mu\text{m}^{-1}$, corresponding to the limits of the BFP. This effect can be identified more clearly in the integrated intensity plot, red line in fig. 3.4, where the intensity follows a trend similar to the one for the random array up to 15 $\text{rad } \mu\text{m}^{-1}$, but the slope becomes more pronounced at larger $k_{||}$. Given the agreement between the experimental results and the 2D Fourier transform, we can use the latter to predict how light will be scattered for momenta larger than the maximum achievable with our setup.

3.2 Zebra patterns

The optimized array of nanoparticles already shows a higher concentration of scattered light in the desired range of k . Nevertheless, we can go further by considering now the optimized texture or zebra pattern, as shown in fig. 1.2 (d), which is tailored to distribute the diffracted light in a narrow range of momenta.

3.2.1 Fabrication

Two different techniques were used for the fabrication of the structures: focused ion beam and electron beam lithography. In both cases we used Si as a substrate. Following the same approach as before, the design of the pattern was made by stitching together several fields, with each unit cell corresponding to the texture shown in 1.2 (d). Even though the original field has a total size of $2 \mu\text{m}$, we can scale it to tune the range of $k_{||}$ such that it fits with the range that we can collect with our Fourier microscope. Therefore, we chose to have unit cells of $4 \times 4 \mu\text{m}^2$, in addition to an extra sample with size $6.5 \times 6.5 \mu\text{m}^2$ to test the scalability in k -space.

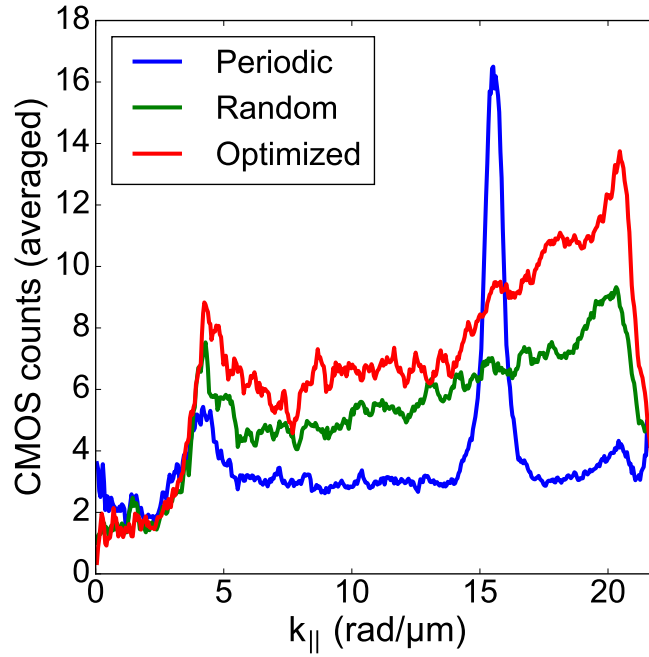


Figure 3.4: **Plot of the number of counts registered on the CMOS sensor integrated over the polar angle as a function of $k_{||}$.** The periodic array (blue) shows a clear peak at $15.6 \text{ rad } \mu\text{m}^{-1}$, corresponding to the first order of the diffraction pattern. The random and optimized patterns (green and red, respectively) exhibit a similar trend for momenta up to $15 \text{ rad } \mu\text{m}^{-1}$, with a slight increase in the intensity. For larger $k_{||}$, the optimized array shows a higher slope in intensity compared to the random one, in agreement with the expected concentration of light in this range.

3.2.1.1 Patterning with FIB

The first attempt to fabricate the zebra pattern was performed by milling a Si substrate with focused gallium ions (Ga^+) (FEI Helios Nanolab 600), which allows to reproduce a given pattern on the substrate. Figure 3.5 shows SEM images of two samples fabricated with this method. The first field (a) is composed of $6.5 \times 6.5 \mu\text{m}^2$ -size unit cells and has a total field size of $20 \times 20 \mu\text{m}^2$, while the second one (b) has $4 \times 4 \mu\text{m}^2$ and $60 \times 60 \mu\text{m}^2$ unit cell and total size, respectively. The parameters used in the fabrication of both are given in table 3.2. We can observe that the zebra pattern is better reproduced in the first field (a), which shows relatively high transitions between the high and low parts of the structure. This is probably due to the fact that the unit cell is larger and, thus, the feature sizes are big ($\sim 200\text{-}300 \text{ nm}$) compared to the achievable resolution. Moreover, when patterning small fields ($20 \times 20 \mu\text{m}^2$) the required magnification in the SEM is larger, which improves the resolution of the final pattern. Instead, the second field (b) exhibits less steep walls, with smoother height transitions. In both cases the height of the structures was less than 90 nm , which was measured by making cross sections with the FIB.

Patterning with FIB allowed us to have a first approach in the fabrication of the optimized textures. However, nanofabrication with this method has several challenges, such as the limited field size that can be patterned due to the large time required ($\sim 3.5 \text{ h}$ for the

Parameters	Field 1	Field 2
Size unit cell	6.5x6.5 μm^2	4x4 μm^2
Size total field	20x20 μm^2	60x60 μm^2
Current	27 pA	27 pA
Voltage	30 kV	30 kV
Dwell time	1 μs	1 μs
Magnification	10000x	3500x

Table 3.2: **Parameters for fabrication of zebra patterns on silicon with focused ion beam.**

60x60 μm^2 field) and the resolution dependence on the magnification. In addition to this, we should take into account the implantation of Ga^+ ions on the substrate and redeposition of the milled material on the structure, which will alter the final result. Hence, we chose electron beam (e-beam) lithography as a next step in the fabrication of the optimized textures.

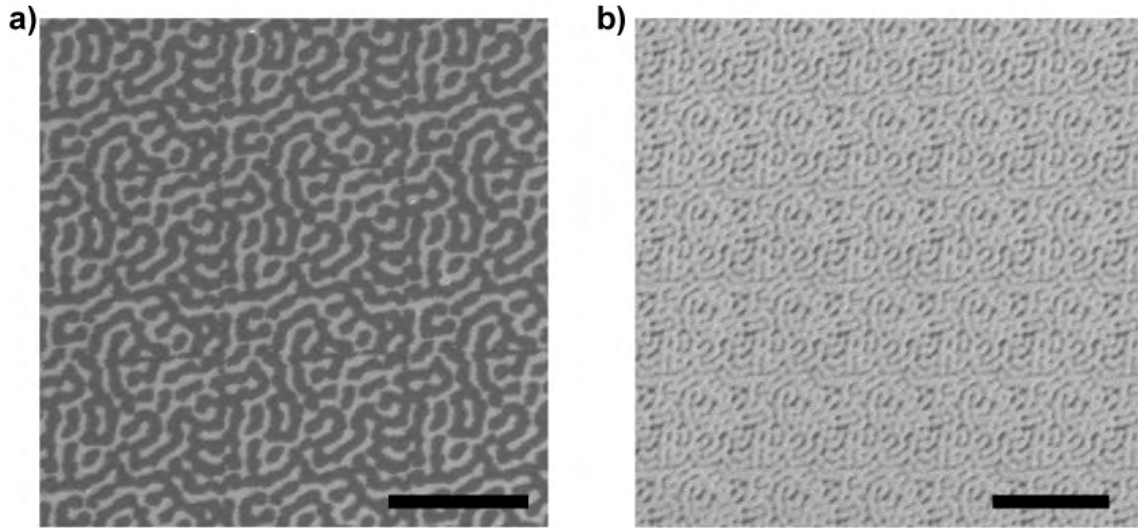


Figure 3.5: **SEM images of the two zebra patterns fabricated with focused ion beam.** (a) Field with a unit cell of 6.5x6.5 μm^2 and total size 20x20 μm^2 . (b) Field with 4x4 μm^2 and 60x60 μm^2 unit cell and total sizes, respectively. The scale bar equals 5 μm in both images.

3.2.1.2 E-beam lithography

Figure 3.6 (a) shows a schematic of the main steps for the fabrication of the zebra pattern using e-beam lithography. In the process, a monolayer primer (HMDS) and photoresist (AR-P 6200/2) are first spin-coated on a clean Si wafer (4000 rpm for 40 and 45 s, respectively). Subsequently, the pattern is written by e-beam lithography (Voyager) using an electron beam energy of 50 keV, 0.4 nA beam current, 20 nm step size and a dose of 100 $\mu\text{C}/\text{cm}^2$. In this case, the patterns consisted of a 200x200 μm^2 field composed of 4x4 μm -size unit cells stitched together in a periodic fashion. Next, the sample is developed and cleaned with a series of chemical compounds (pentyl acetate, o-xylene, methyl isobutyl ketone (MIBK):isopropyl alcohol (IPA) (9:1) and IPA). Plasma etching is needed

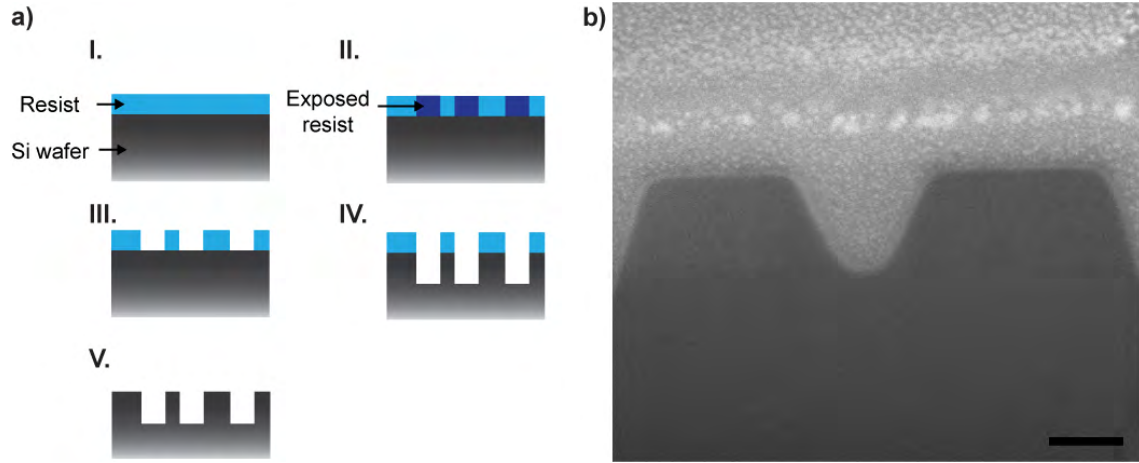


Figure 3.6: **Fabrication of the zebra pattern with e-beam lithography.** (a) Schematic of the main steps in the nanofabrication process: a thin layer of photoresist is spin-coated on a Si wafer (I) and patterned with e-beam lithography (II). Subsequently, the exposed resist is developed (III) and plasma etching is used to etch the Si (IV). Finally, the remaining resist is removed (V). (b) Cross section of the fabricated structure, showing a height of approximately 200 nm. The scale bar indicates 100 nm and the grains on top of the structure correspond to the deposited Pt.

Parameters	Oxide etch	Si etch
Gases	Cl ₂ : 50 sccm	HBr: 48 sccm O ₂ : 2 sccm
Pressure	7 mTorr	7 mTorr
HF: Forward power	30 W	30 W
ICP: Forward power	750 W	750 W
Temperature	60 °C	60 °C
Etching time	11 s	80 s

Table 3.3: **Parameters of plasma etching (RIE) for native oxide and Si etch.**

to first remove the native and then etch the Si to obtain the desired height, with the details shown in table 3.3. Finally, the remaining photoresist is removed with base piranha. Figure 3.6 (b) shows a cross section of the structure, from which we can obtain that the height of the features is around 200 nm, which is much higher than the structures obtained with FIB. The SEM images of the complete structure are shown in fig. 3.7, from the top (a) and from an angle of 52° (b). We can observe that now the sides of the structures are sharp, with clear transitions between the low and high regions (dark and bright respectively in fig. 3.7 a).

3.2.2 Discrete 2D Fourier transforms

We can now perform again discrete 2D Fourier transforms of the SEM images of the fabricated patterns. Figure 3.8 shows the top view of the two samples fabricated with FIB (a, b) and the one done using e-beam lithography (c), together with their corresponding Fourier transforms (d-f). We will refer to these fields as 1, 2 and 3, respectively. The Fourier maps exhibit in the three cases a ring with high intensity compared to the rest of

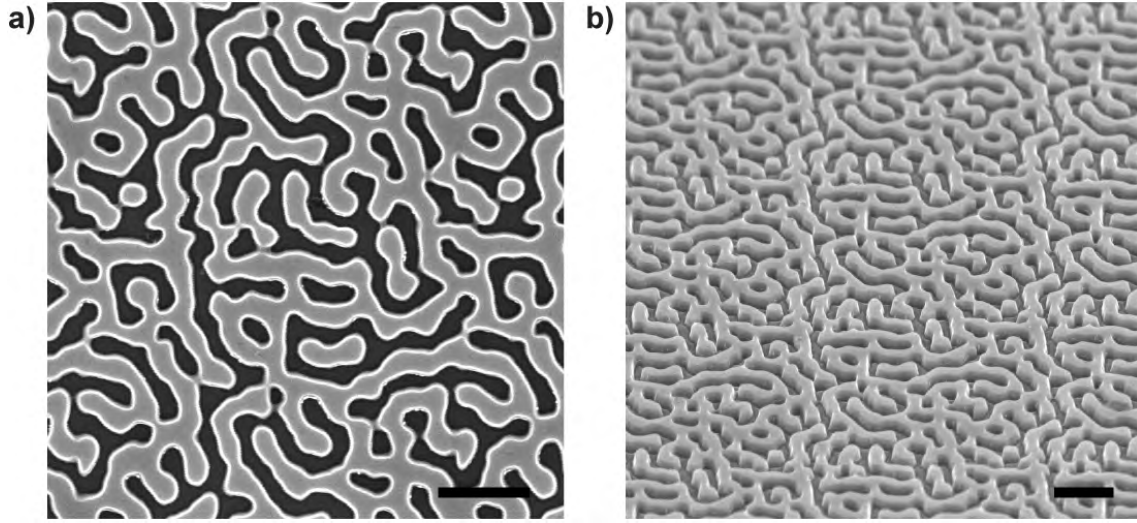


Figure 3.7: **SEM images of the zebra pattern fabricated with e-beam lithography.** (a) Top view and (b) perspective from an angle of 52° . In both cases the scale bar indicates $1\ \mu\text{m}$. In the top view, the dark areas correspond to the etched Si, while the bright areas have a height of $200\ \text{nm}$.

the map, which matches with the expected distribution from the theoretical zebra pattern, as depicted in fig. 1.2 (d). In particular, field 1, with $6.5 \times 6.5\ \mu\text{m}^2$ unit cell-size, exhibits a higher intensity in the range of $7\text{-}11\ \mu\text{m rad}^{-1}$, while the other two show a ring comprising the range of $12\text{-}17\ \mu\text{m rad}^{-1}$. This is in accordance with the expected scalability of the Fourier transform as a function of the size of the pattern. Moreover, we should notice that this scalability also affects the width of the ring: large patterns allow for concentration of light in a narrower range of $k_{||}$. In addition to this, when comparing the maps of fields 2 and 3, which have the same unit cell but different fabrication method (e and f), we can observe significant differences. Field 2 (e) shows a concentration of diffracted light within the mentioned range of $k_{||}$, but the intensity exhibits a non uniform distribution inside this range, being higher over one of the diagonals. This effect can already be seen in the initial design by van Lare (1.2, d), but becomes less noticeable in the Fourier transform of field 3. The latter shows an almost equivalent distribution in all directions. Furthermore, it exhibits less intensity at low $k_{||}$ compared to the sample fabricated with FIB, while the scattering at large momenta is higher than in fields 1 and 2.

Lastly, we should notice that the shapes in the Fourier maps that we describe are always composed by discrete intensity peaks instead of a continuum. This effect is due to the fact that our samples are constituted by a periodic arrangement of small fields, and therefore we can observe the diffraction pattern of this periodic arrangement. In particular, the peaks have an average spacing of $\sim 1\ \mu\text{m rad}^{-1}$ in field 1, which would correspond to an average periodicity in real space of $\Lambda = 2\pi/1\ \mu\text{m rad}^{-1} = 6.3\ \mu\text{m}$ that matches closely with the $6.5\ \mu\text{m}$ of the unit cell.

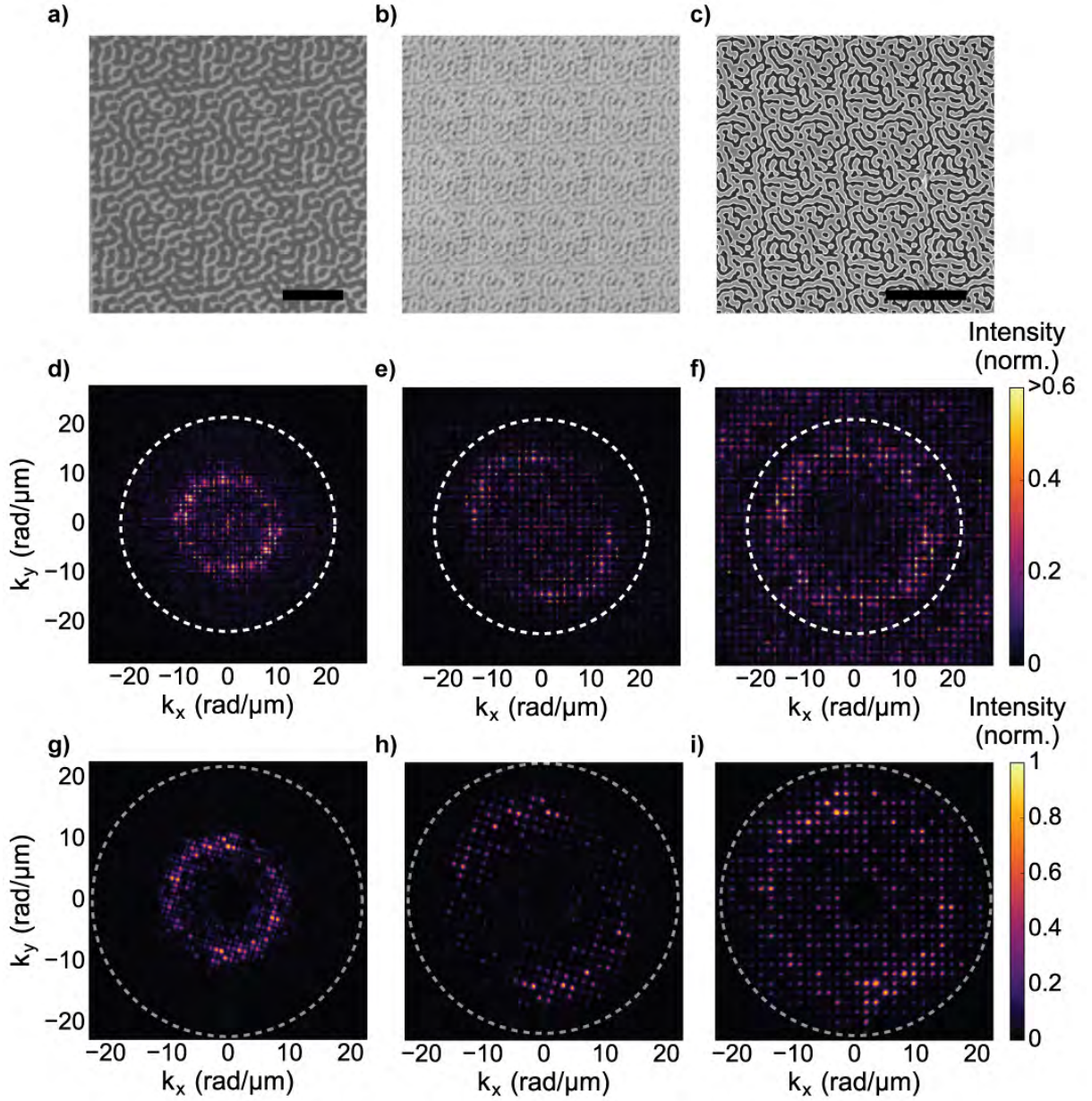


Figure 3.8: **SEM images of the fabricated zebra patterns seen from the top and their corresponding discrete 2D Fourier transform and Fourier microscopy images.** (a-c) Top view SEM images of the fields fabricated with FIB (a, b) and e-beam lithography (c). The first field is composed by a unit cell of $6.5 \times 6.5 \mu\text{m}^2$, while the other two have $4 \times 4 \mu\text{m}^2$ -size unit cells. The scale bars indicate $4 \mu\text{m}$. (d-f) 2D discrete Fourier transforms of the SEM images. The white dashed line indicates the maximum range of $k_{||}$ that can be obtained with our Fourier microscope. All of the fields show a concentration of intensity within a certain ring in the k -space, in the range $7\text{-}11 \mu\text{m rad}^{-1}$ for field 1 (d) and $12\text{-}17 \mu\text{m rad}^{-1}$ for fields 2 and 3. The corresponding diffraction patterns obtained with the Fourier microscope (g-i) agree very well with the discrete Fourier transforms.

3.2.3 Measurements

Finally, we can test the distribution of the light scattered by the fabricated samples using the Fourier microscope. Figure 3.8 (g-i) shows the resulting diffraction patterns, where the

white dashed circle indicates again the maximum $k_{||}$ that can be captured. Additionally, in fig. 3.9 we also plot the number of counts on the CMOS sensor, which is integrated over the polar angle, as a function of $k_{||}$. In general we can observe that the measurements agree very well with the previous discrete Fourier transforms, reproducing perfectly the scales in k -space and the distribution of the intensity, in addition to the periodic diffraction effects coming from the unit-cell repetition. Therefore, this proves that the zebra pattern has a clear scattering pattern corresponding to a ring in a range of $k_{||}$, which can be tuned with the field size.

If we look closely at the different fields, we can observe that field 1 shows a high and narrow intensity peak at $k_{||}$ around $8.7 \mu\text{m rad}^{-1}$, as shown in fig. 3.9 (blue line). In the same fashion, field 2 (green line) shows a high intensity in the expected range ($12\text{-}17 \mu\text{m rad}^{-1}$), even though lower than the rest of the fields, and the Fourier image (fig. 3.8, h) exhibits again a non uniform distribution of the intensity over the ring in $k_{||}$, with higher intensity over one of the diagonals. The latter is in agreement with the 2D Fourier transform of the same field and suggests that comes from the fabrication of this pattern. Interestingly, in this case the intensity at low $k_{||}$ is lower than the one expected according to the discrete Fourier transform. Lastly, the intensity distribution of field 3 (fig. 3.9, red line) corresponds to the same range of $k_{||}$, but in this case is higher than for field 2. Moreover, we should notice that this field in general has a higher intensity offset compared to the two previous ones. This could be due to the fact that the structure is higher than the samples fabricated with FIB, and therefore the scattering strength might vary with different heights [14].

3.3 Discussion and outlook

In this chapter we have shown that we can tune the direction, and therefore momentum, of the diffracted light by changing the shape and distribution of arrays of nanoparticles or textures, such as the zebra pattern. So far, we have not addressed the diffraction efficiency, i.e., the ratio between light diffracted into the desired direction and total incoming light [17]. If we consider the limit case in which the height of the nanopattern is zero, there is only reflection and, therefore, only the zero diffraction order is present, while increasing the height leads to the exhibition of higher diffraction orders. Hence, we expect that the height of our nanopatterns will have a significant role in determining the diffraction efficiency. In a similar fashion, until now we have only considered patterns constituted by the same material, Si in our samples, but we could also think of fabricating structures of a given material on top of a different one, as we will consider in the next chapter. In this case, the optical constants and, therefore, reflectivity of each material are different, meaning that we add an extra parameter to tune the diffraction efficiency.

Apart from the diffraction efficiency of the nanopatterns, it is also important to consider the spatial coherence of light. In our approach, the scattering of light into the desired range of $k_{||}$ is possible thanks to the constructive and destructive interferences of light scattered at different positions on the nanopattern. Therefore, this redirection will only take place if the incident light has a coherence length of at least the size of the diffraction pattern, i. e., the phase of the light at different points of the sample needs to be correlated for a distance

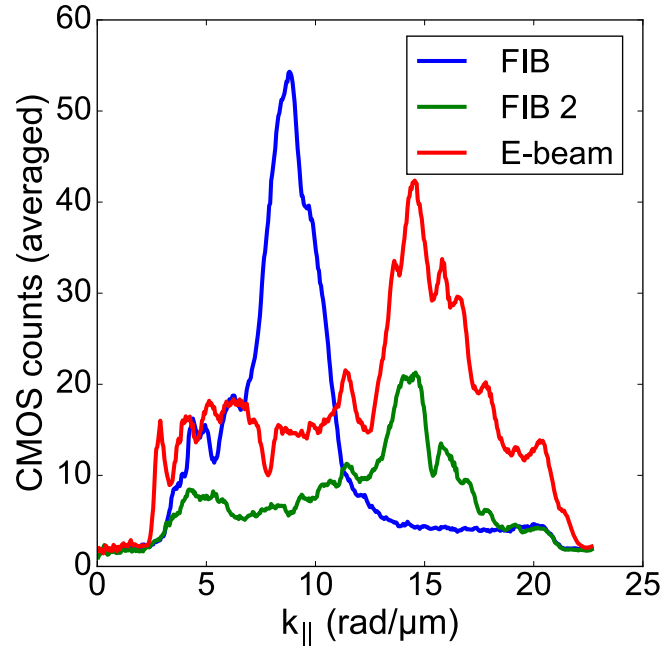


Figure 3.9: **Plot of averaged number of counts on the CMOS sensor as a function of $k_{||}$ for the three fabricated patterns.** Field 1 (blue), corresponding to a unit cell of $6.5 \times 6.5 \mu\text{m}^2$, shows a clear peak at $8.7 \mu\text{m rad}^{-1}$, while fields 2 and 3 (green and red, respectively), with unit cell of $4 \times 4 \mu\text{m}^2$, show an intensity distribution in the range $12\text{-}17 \mu\text{m rad}^{-1}$. The field fabricated with e-beam lithography exhibits in general a higher intensity, probably due to the larger height of the structures in comparison to the samples fabricated with FIB.

equal or larger than the size of the patterns [18]. Otherwise, light at different positions will be scattered independently and no diffraction pattern will be formed. Divitt and Novotny recently showed that the coherence length of sunlight can vary from around 80λ , where λ is the wavelength, for direct light down to 7λ for highly diffuse sunlight [19]. Consequently, when optimizing or scaling the nanopatterns that we have shown we should always take into account that the size of a unit cell should be equal or smaller than this coherence length.

Chapter 4

APPLICATIONS IN SOLAR CELLS

Once we have shown the distribution of light in the k -space by the different nanopatterns, we can study and optimize their effect when applied to solar cells. In this chapter, we first show the coupling of light into waveguide modes through a CIGSe solar cell with a patterned periodic array, which leads to an absorption enhancement in the final fabricated cell. As a further step, we use FDTD simulations to evaluate the effect in the total absorption of a CZTS solar cell.

4.1 Periodic arrays for light trapping in CIGSe solar cells

$\text{CuIn}_{1-x}\text{Ga}_x\text{Se}_2$ (CIGSe) solar cells are promising candidates to compete with Si photovoltaics thanks to their increasing development in the last years, achieving a record efficiency of 22.7 % [20]. However, in order to further reduce the fabrication cost and usage of material, we can still decrease the absorber thickness, which is currently 2.5-3 μm for the world record [21], while tackling the consequent loss in absorption. It has been shown that adding dielectric nanoparticles at the rear of 400-500 nm-thick CIGSe layers improves the overall absorption of the solar cell [5, 8]. In particular, an efficiency enhancement from 6.8 % for the flat cell to 10 % for the nanopatterned one was measured.

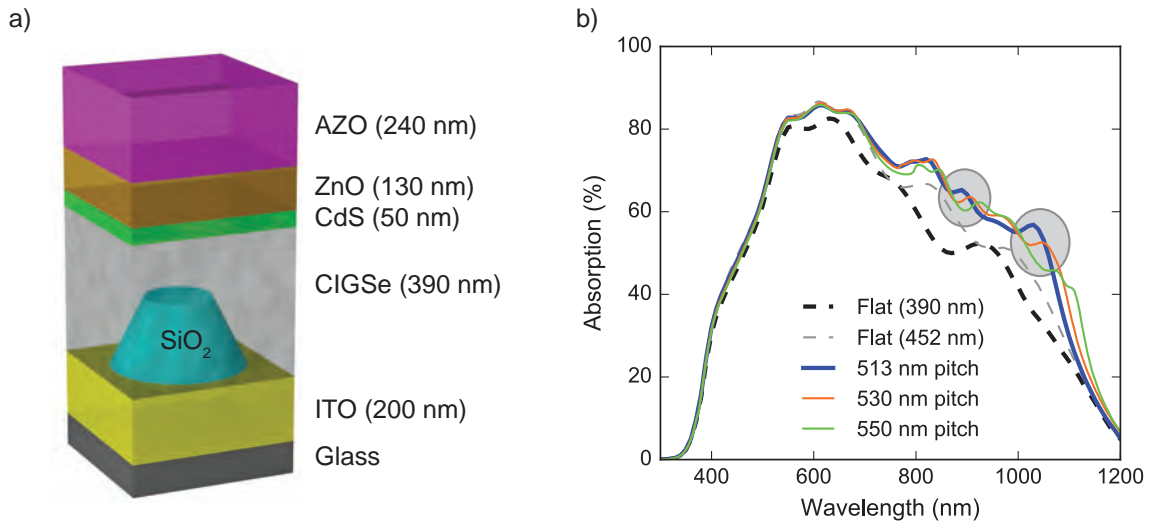


Figure 4.1: Absorption enhancement in CIGSe solar cells with a periodic array of dielectric nanoparticles. (a) Schematic of a unit cell of the modelled solar cell geometry. (b) Modelled absorption in the CIGSe layer for a 390 nm-thick flat cell and a patterned cell with the 452 nm thickness and nanoparticle pitch of 513 (corresponding to the experimental one), 530 and 550 nm. The absorption for a 452 nm-thick flat cell is also shown to compare with the Fabry-Pérot resonances. Fig. (a) and the data from (b) have been extracted from ref. [5].

The absorption in the CIGSe layer can be modelled using finite-difference time-domain

(FDTD) simulations [22]. The unit cell of the modelled geometry is shown in fig. 4.1 (a), where the absorber has a thickness of 390 nm and the SiO₂ nanoparticles, with bottom and top diameter of 102 and 205 nm, respectively, and 210 nm height, are distributed in a periodic array with pitch 513 nm. Figure 4.1 (b) shows the absorption spectrum for a flat cell (dashed black) and a cell containing the periodic array of nanoparticles (blue). In both cases the volume of the absorber is preserved, and thus the thickness is increased for the cell containing the particles. We can observe that for wavelengths larger than 600 nm the absorption of the nanopatterned cell increases with respect to the planar one. Moreover, when changing the pitch from 513 to 530 (orange) and 550 nm (green) we observe that the absorption spectrum changes, with two main peaks at 900 nm and 1050 nm that red shift for increasing pitch, as indicated in the figure.

In order to further understand the origin of this enhancement, in this thesis we studied the effect of coupling of the light scattered by the nanoparticle array to the waveguide modes supported by the CIGSe layer. The optical data of the constituent materials in a CIGSe solar cell are shown and discussed in appendix B.1.1. The high refractive index of CIGSe allows it to support several optical waveguide modes. In particular, we can obtain their dispersion relations, thus relating the wavelength of the light propagating inside the material with the in-plane wavevector of the mode, $k_{\text{waveguide}}$, which is equivalent to the parallel momentum k_{\parallel} that we have been considering in the previous chapters. Fig. 4.2 (a) shows the dispersion relations of the lowest-order transverse electric and magnetic modes (TE and TM, respectively) supported by a planar structure such as the one shown in 4.1 (a) but without the SiO₂ nanoparticles. The relations were calculated by means of the transfer matrix method [23] and do not account for the uncertainty in the value of k_{\parallel} due to the absorption of the material, which should have an effect mainly at short wavelengths where the absorption coefficient is high. This *uncertainty* accounts for the fact that in an absorbing medium we can excite a certain waveguide mode within a certain range of wavevectors, with this range increasing for high absorption [24]. Higher orders can also be found but the electric and magnetic fields are no longer entirely confined inside the absorber layer. We can observe this confinement of the fields by plotting them as a function of the depth in the structure. Fig. 4.2 shows the electric field profile of the electric modes, TE0 (red), TE1 (blue) and TE2 (yellow) for a wavelength of 850 nm, together with the corresponding refractive index at each layer for this wavelength (c). All of the fields are confined inside the CIGSe layer, with only a small leakage into the adjacent layers for the TE2 mode.

We can increase the path of the light inside the material, and thus the probability of being absorbed, by exciting these modes by the incoming light. For this purpose, we need to match the momentum of the light with the corresponding wavevectors of the modes. This momentum can be provided by the periodic array of nanoparticles and follows the grating equation presented in eq. 2.5, which depends on the pitch of the grating and the different diffraction orders. In particular, the momentum provided by the [10] order of the 513 nm-pitch array is $12.3 \text{ rad } \mu\text{m}^{-1}$, which coincides with the TE1 and TE2 modes at wavelengths around 1050 and 900 nm, as indicated in fig. 4.2 (a, blue dots). These wavelengths match with the ones where we observed an enhancement in the absorption of CIGSe (fig. 4.1, b), indicating a possible coupling between the scattered light and the waveguide modes.

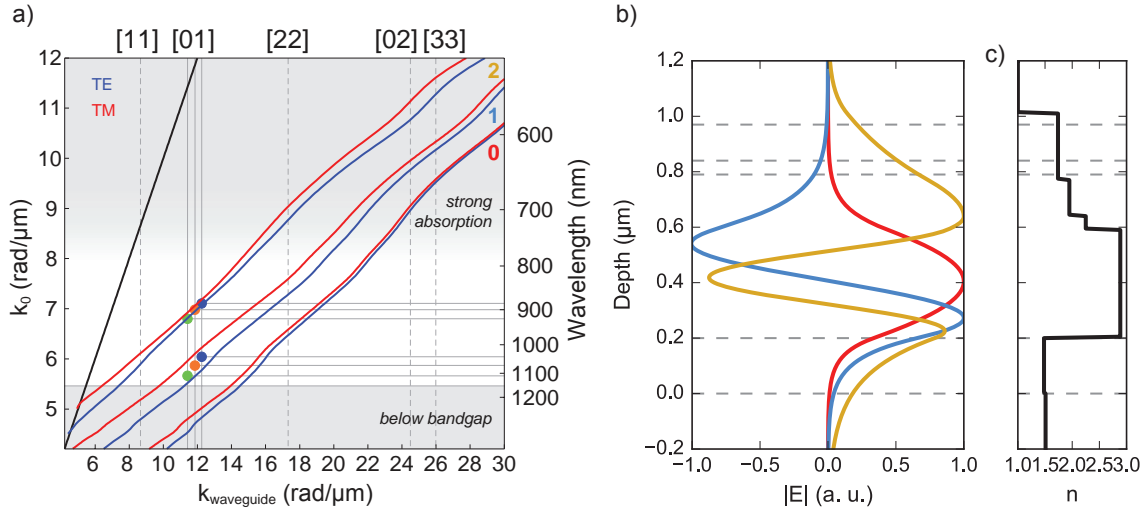


Figure 4.2: **Fundamental waveguide modes of a planar CIGSe solar cell.** (a) Dispersion relations of the lowest-order transverse electric and magnetic modes (TE and TM, respectively) for a planar structure as the one shown in 4.1 (a) without nanoparticle arrays. The momentum provided by the periodic arrays of nanoparticles match with the wavevectors of the bounds at the wavelengths where we see an enhancement in the absorption, thus suggesting possible coupling to waveguide modes. (b) Electric field distributions at 850 nm of the TE0 (red), TE1 (blue) and TE2 (yellow) as a function of the depth in the structure, together with the corresponding refractive index at each layer (c). The fields are completely confined inside the CIGSe layer, except for a small leakage into the adjacent layers for the TE2.

Moreover, the arrays with pitch 530 and 550 nm also match the wavevectors of the modes at the wavelengths with absorption peaks, thus offering a further proof of this coupling. Finally, we should consider that the TE0 also matches the [01] order of the array but only at wavelengths above the band gap, thus absorption is not possible. Other orders, such as the [11] and [22], could also be coupled to the wavevectors, but no effect is shown in the absorption spectrum, probably due to their lower diffracting efficiency due to the form factor (discussed in section 3.1.2 and ref. [16]). In addition to this, we should also notice that even though we calculated the dispersion relations for a planar cell, we can still observe a momentum matching between modes and scattered light, indicating that the modes of the planar geometry are not significantly perturbed by the presence of the nanoparticles.

4.2 Zebra patterns for light trapping in CZTS solar cells

Following the same idea as for the periodic arrays of nanoparticles, we can now use the zebra patterns to enhance light trapping in thin film solar cells and study its coupling to waveguide modes. Even though the approach can be applied to any photovoltaic material, we evaluated its effectiveness by considering $\text{Cu}_2\text{ZnSnS}_4$ (CZTS) solar cells, which are increasingly gaining interest due to their earth-abundant composition and band gap close to the optimum one according to the Shockley-Queisser limit [25]. In particular, we focused on the solar cells developed by the group of Dr. Xiaojing Hao, from the University of New South Wales (UNSW Sydney), which currently holds the world record in efficiency

(9.2 %) for thin film pure sulfide CZTS cells [20, 26]. The geometry of these solar cells is shown in figure 4.3 (a), where the absorber has a thickness of around 800 nm and it is fabricated on top of a molybdenum-coated glass substrate. On top of the CZTS layer thin buffer layers, $\text{Zn}_{0.35}\text{Cd}_{0.65}\text{S}$ and ZnO, are grown, together with a 200 nm-thick indium tin oxide (ITO) film. The complete experimental details can be found in ref. [26]. The measured external quantum efficiency (EQE) for this device is shown in fig. 4.3 (b), where the red and black lines refer to a device with $\text{Zn}_{0.35}\text{Cd}_{0.65}\text{S}$ and CdS as buffer layer, respectively. Even though the one with $\text{Zn}_{0.35}\text{Cd}_{0.65}\text{S}$ showed a higher power conversion efficiency, the performance at wavelengths larger than 600 nm decays more rapidly. In order to improve the overall efficiency, we aim to optimize light trapping in this wavelength range.

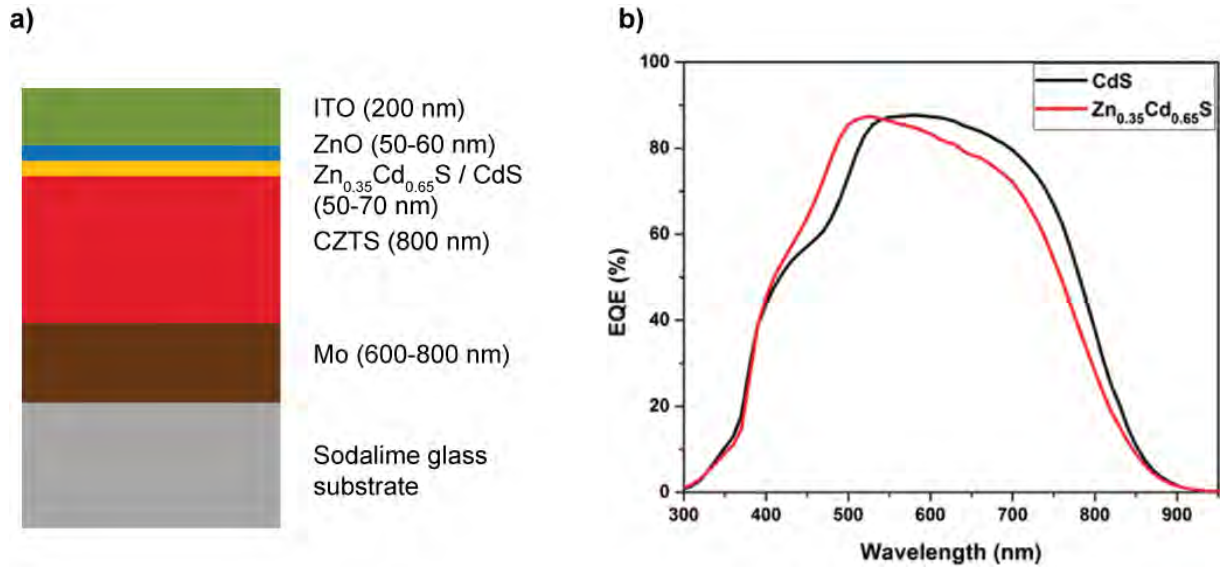


Figure 4.3: **EQE measurements for CZTS solar cells with different buffer layers.** (a) Geometry of the CZTS solar cell that we will study, together with the measured EQE of the device (b) for two different buffer layers. We will aim to improve light trapping for wavelengths larger than 600 nm, where the EQE exhibits a poorer performance. The EQE plot was obtained from ref. [26].

4.2.1 Waveguide modes supported by a CZTS solar cell

The optical data for the constituents materials of the CZTS solar cells is shown and discussed in the supplementary information (sec. B.1.2). CZTS has a high refractive index compared to the rest of materials that constitute the cell, and therefore we know that it can support a set of confined waveguide modes. Hence, we can calculate again the dispersion relations via the transfer matrix method [23]. Given that we want to enhance light trapping while reducing the amount of absorber, we consider now a thickness of 400 nm for the CZTS layer, as depicted in fig. 4.4 (b). The calculated waveguide modes are shown in fig. 4.4 (a), where the blue and red lines represent transverse electric (TE) and magnetic (TM) modes, respectively. In particular, we plot three pairs of TE and TM modes (TE₀/TM₀, TE₁/TM₁ and TE₂/TM₂), with the lowest ones always corresponding to the ones with higher values of wavevector, $k_{\text{waveguide}}$, as indicated on top of the figure. The dashed lines indicate the limit wavevectors for bound modes inside each material and

are calculated by:

$$k_{\text{waveguide}}(k_0) = k_0 n_{\text{material}}(k_0) \quad (4.1)$$

where n_{material} refers to the real part of the refractive index of the material. Hence, when looking at a certain mode, the dashed lines on the right indicate in which layers it can propagate. Hence, according to the plot, at $\lambda=600$ nm mode 0 can only propagate inside the CZTS layer and, therefore, is complete confined. Instead, TE1 and TM1 can also propagate inside both the CZTS and CdS, while TE2 and TM2 would not propagate anymore inside the CZTS but would be absorbed by the Mo. Higher order modes have been neglected since they do not propagate any more inside the CZTS layer.

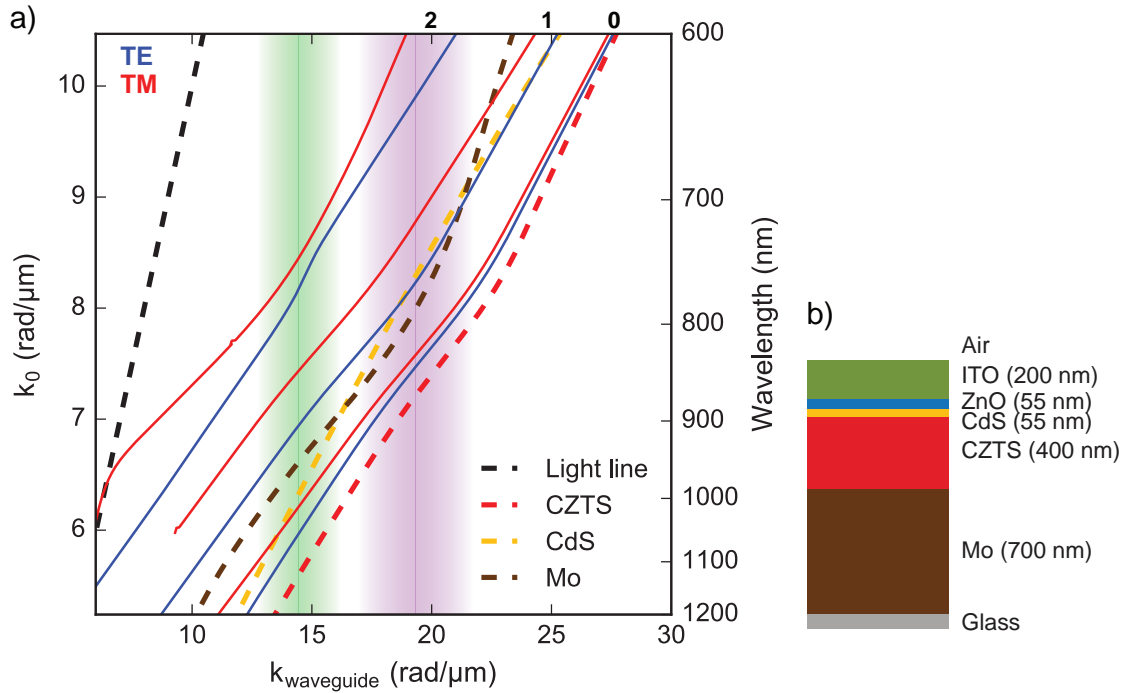


Figure 4.4: Dispersion relations of the fundamental modes in a CZTS solar cell. The blue and red lines indicate transverse electric (TE) and magnetic (TM) modes, and the numbers on top refer to the orders of the pairs of modes. The dashed lines indicate the limits for bound modes in each material. Higher order modes have been neglected since they propagate mainly inside the Mo layer. The range of $k_{\text{waveguide}}$ that can be scattered by the zebra patterns is indicated in green, corresponding to a pattern with total size 4x4 μm², and magenta, for a 3x3 μm²-field.

To elucidate further the confinement of the modes inside the different layers, we plot the electric field profiles as a function of the depth in the structure for the three main TE modes at $\lambda=600$ nm (fig. 4.5). We observe that in all cases the electric field is confined inside the CZTS layer, with only a small leakage towards CdS and ZnO. We should notice that the TE2 should not be confined inside the CZTS layer according to its dispersion relation, but here we obtain that it is still mainly bound inside this layer. This is probably due to the high absorption of CZTS at this wavelength, which implies that the excitation of a waveguide mode is possible in a relatively broad range of momenta $k_{\text{waveguide}}$, as discussed in the previous section. This effect should become negligible for increasing wavelengths,

meaning that we can still rely on the results from the dispersion relations. Moreover, we should always consider that this confinement will depend on the wavelength and therefore the higher modes might not be bound in the CZTS layer any more for larger wavelengths.

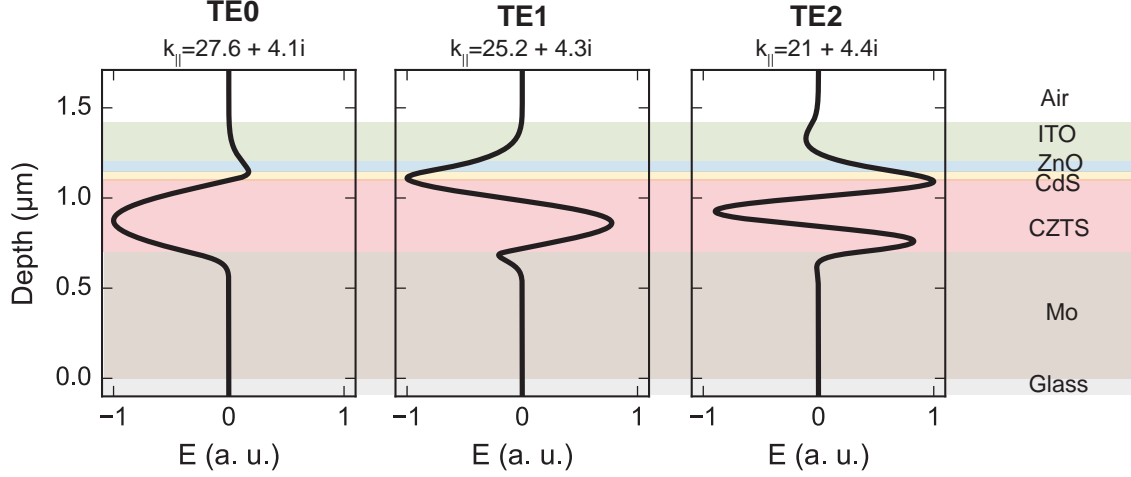


Figure 4.5: **Electric field profiles of the fundamental transverse electric modes at $\lambda=600$ nm.** The electric fields are normalized and plotted as a function of the depth inside the structure. The three modes are confined mostly inside the CZTS layer, which is desirable for light trapping applications.

4.2.2 Light trapping with zebra patterns

Once we know the dispersion relations of the modes supported by the CZTS cells, we can evaluate and optimize the effect of the zebra patterns for light trapping purposes. Following the same idea as for the CIGSe, we want to add a scattering pattern at the rear of the CZTS layer, on top of Mo, such that the light that is not absorbed after the first pass inside the film will be scattered towards certain directions, i.e., wavevectors $k_{||}$, matching the waveguide modes. Therefore, we want patterns to be made of a non-absorbing material with a relatively low refractive index compared to CZTS. In particular, we chose silica (SiO_2), which can be easily included in the fabrication process by simply spin coating sol-gel, as done in the SCIL process, or evaporating it on top of the Mo-coated glass substrate and then etching to obtain the desired pattern. Figure 4.6 (b) depicts the geometry of a simulated CZTS solar cell with a zebra pattern. Notice that when we add these patterns, we still want to maintain the same amount of absorber volume and, therefore, we will increase the thickness of CZTS accordingly, which in this case corresponds to 500 nm.

Taking into account the EQE (fig. 4.3, b) and absorption coefficient (appendix B.2, b) spectra, we chose to optimize the light trapping for wavelengths larger than 700 nm. Therefore, considering the dispersion relations in fig. 4.4, this means that the zebra pattern should provide wavevectors smaller than $23 \text{ rad } \mu\text{m}^{-1}$, approximately. We can match these wavevectors with the ones scattered by the zebra patterns by considering the Fourier microscopy measurements from chapter 3, and in particular fig. 3.9. Specifically, we focus on the pattern fabricated with e-beam lithography, since it allows for large area fabrication. The range of $k_{||}$ in which a $4 \times 4 \mu\text{m}^2$ -size zebra pattern scatters is indicated in

fig. 4.4 as a green area. The centre and width of this region correspond to the position of the maximum and full width half maximum (FWHM) of the fitted main peak that we obtained in the measurements (fig. 3.9, red line). Thus, we can see that this zebra pattern matches the wavevectors of the fundamental modes confined inside the CZTS (TE₀, TM₀, TE₁ and TE₁) at wavelengths larger than 900 nm. Therefore, it could be a good option to improve light trapping at very large wavelengths, but we should take into account that the absorption is also very small in this range, and therefore, the light trapping effects might be negligible. In contrast, we could also think of a smaller field to embrace larger $k_{||}$. The magenta area in fig. 4.4 shows the range covered by a $3\text{ }\mu\text{m}^2$ -size zebra pattern. In this case, the scattering is centred at around $19\text{ rad }\mu\text{m}^{-1}$, which would allow for momentum matching with the bound modes between 650 and 900 nm. Moreover, we should notice that in this case the FWHM, and therefore the range of $k_{||}$, is wider since it also scales when resizing the entire pattern.

As a next step we can perform 3D FDTD simulations to model the absorption spectrum of the CZTS layer from the discussed solar cell geometry. The models were developed by considering the optical data shown in 4.6 (b) and in all simulations we used a mesh size of 5 nm to guarantee full convergence. We obtained a complete spectrum from 400 to 1200 nm, with steps of $\Delta\lambda=20\text{ nm}$. This was done by performing a set of simulations, each of them with a plane wave with central wavelength λ and span 20 nm as a source, with normal incidence on the cell. The fraction of light absorbed inside a given layer can be extracted by obtaining the total flux in that film.

Figure 4.6 (b) shows the modelled absorption of CZTS (solid) and Mo (dashed) for four different geometries: two planar ones, with 400 and 500 nm-thick absorbers (black and grey), together with two zebra patterns with sizes 4×4 and $3\times 3\text{ }\mu\text{m}^2$ (green and magenta, respectively). We first focus on the reference cell, which corresponds to the planar geometry with thickness 400 nm. It exhibits low absorption ($\sim 40\%$) for wavelengths in the range 400 to 550 nm, probably due to the peak in absorption of CdS in this range (fig. B.2). This hypothesis is supported by the fact that the absorption in Mo is zero, meaning that almost no light reaches this layer. From 550 until around 650 nm the absorption in CZTS seems reasonable, with an average of around 70-75 %, and Mo exhibits again zero absorption. Therefore, the main losses in this region are probably due to the reflection and absorption in the layers above CZTS. In contrast, at larger wavelengths the absorption in CZTS decreases, while increasing in Mo, thus suggesting an inefficient absorption in this range. In addition to this, we can observe Fabry-Pérot resonances in both the CZTS and Mo layer, which rely on the interference of light reflected at the boundaries of perfectly smooth layers. However, in real solar cells the layers can have rough surfaces, meaning that the phase correlation between the incident light and the one scattered by the surface might be lost, and therefore no interferences can take place.

When we add zebra patterns at the rear of the CZTS layer, we observe an enhancement in the absorption for wavelengths longer than 650 nm. In particular, the $4\times 4\text{ }\mu\text{m}^2$ -patterned cell (green curve) exhibits better performance than the planar one in the spectral range 600-700 nm. This effect would not be expected from the dispersion relations (fig. 4.4,

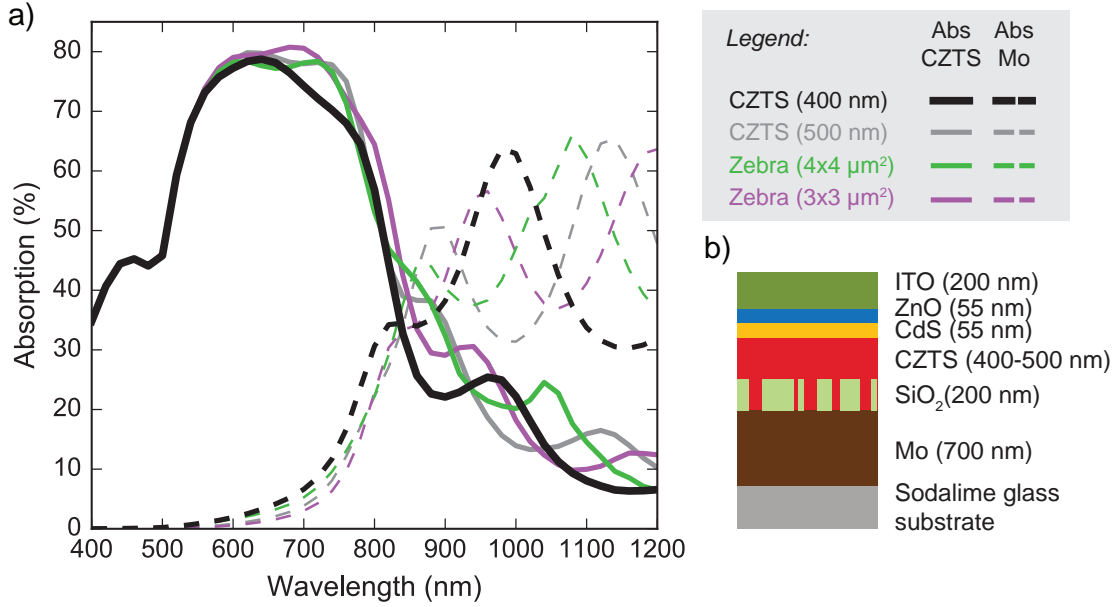


Figure 4.6: **Absorption enhancement in CZTS solar cells with dielectric zebra patterns.** (a) FDTD simulations of the absorption in CZTS (solid line) and Mo (dashed line) for four different cell geometries: planar with 400 nm and 500 nm-thick absorber (black and grey, respectively) and cells containing zebra patterns with sizes 3x3 and 4x4 μm^2 (green and magenta). In the latter, the thickness of CZTS has been increased to 500 nm to maintain the total volume of absorber. The patterned cells show an enhanced absorption with respect to the planar ones, specially at long wavelengths. (b) Geometry of the solar cells used in the simulations.

a), since there are not confined modes inside the CZTS layer that overlap with scattering of the zebra patterns. Nevertheless, this enhancement could come from the fact that the zebra pattern not only redirects light in the desired wavevectors, but also reflects part of the light, which corresponds to the zero-order component that has been blocked in the Fourier microscopy measurements. Therefore, besides the coupling to the waveguide modes we have to account for this doubled path length inside the CZTS layer. In addition to this, we can also see absorption enhancements in the ranges from 800 to 900 nm and 1000 to 1200 nm, which match with the expected coupling to waveguide modes. We should also notice that the absorption becomes smaller than for the reference cell in the range from 950 to 1000 nm, which could be due to a film interference effect originated from the reflection of light due to the zero diffraction order.

If we now look at the 3x3 μm^2 -patterned cell (magenta curve), we observe that the absorption is again improved but in slightly different spectral ranges. The most significant improvement can be seen in the entire range from 600 to 1050 nm, where the absorption becomes higher than for the rest of the curves. This is in agreement with the presence of waveguide modes in this entire range, together with the fact that the range of wavevector affected by this zebra pattern is wider. Additionally, we can observe another broad peak for wavelengths larger than 1100 nm, which is probably not due to coupling to waveguide modes, since there are no modes matching the wavevectors of the zebra pattern in this range, but an interference effect. Finally, since the simulations with zebra patterns are

	J_{sc} ($E_{BG}=1.5$ eV)	J_{sc} ($E_{BG}=1.03$ eV)
Reference (t=400 nm)	17.24 mA/cm ²	20.59 mA/cm ²
Zebra (4x4 μm^2)	17.41 mA/cm ²	21.86 mA/cm ²
Zebra (3x3 μm^2)	17.96 mA/cm ²	21.93 mA/cm ²

Table 4.1: **Calculated short current densities for the reference and patterned CZTS solar cells.** The current densities have been calculated considering two band gaps: 1.5 and 1.03 eV, corresponding to the value found in the literature and the actual value up to which there is still absorption. In both cases, the patterned cells show an enhanced J_{sc} compared to the reference one, specially for the lowest band gap. The cell patterned with a 3x3 μm^2 exhibits a higher current density.

performed with absorber thickness of 500 nm in order to maintain the volume of absorber, we also plot the absorption curve for a 500 nm-thick planar solar cell (grey). It is important to consider this curve to guarantee that the effects that we are discussing do not come only from Fabry-Pérot resonances of a layer with this thickness. Nevertheless, we can already observe that the corresponding absorption curve does not follow the same trend as the ones for the zebra patterns, thus supporting the fact that the enhancement are due to the presence of these dielectric patterns.

In order to evaluate the effect of the zebra patterns in a more quantitative way, we can also calculate the maximum short current density, J_{sc} that can be generated through the following expression:

$$J_{sc} = q \int_{\lambda_0}^{\lambda_{BG}} \frac{I_{Sun}(\lambda)A(\lambda)}{hc/\lambda} d\lambda \quad (4.2)$$

where q is the electron charge, λ_0 is the minimum wavelength of the spectrum, λ_{BG} refers to the wavelength corresponding to the band gap of CZTS, $I_{Sun}(\lambda)$ is the solar spectral intensity, $A(\lambda)$ is the fraction of absorbed light per each cell, h is Planck's constant and finally c corresponds to the speed of light in vacuum. The results for the reference cell (400 nm – thick) and the two patterned ones are summarized in 4.1 (1st column), which have been calculated for a band gap of 1.5 eV ($\lambda_{BG}=826$ nm) extracted from the literature [26, 27]. In this case, the cell patterned with the 3x3 μm^2 zebra pattern exhibits an enhancement of 4 % with respect to the reference one. Nevertheless, from fig. 4.6 (a) we observe that a significant proportion of the light is absorbed at wavelengths larger than 826 nm and, therefore, we should account for it when calculating J_{sc} . The results considering a band gap of 1.03 eV ($\lambda_{BG}=1200$ nm) are shown in table 4.1 (2nd column). Now, the patterned cells show a 6 % increase in J_{sc} with respect to the planar one, with the highest value of current density corresponding to 21.93 mA/cm² for the 3x3 μm^2 zebra pattern.

4.3 Discussion and outlook

In this chapter we have taken a step forward in the use of optimized patterns for light trapping purposes by showing the enhancement in absorption of nanopatterned thin film

solar cells. Both the experimental results from the periodically-patterned CIGSe cells and the simulations for CZTS solar cells with zebra patterns exhibit the coupling of light scattered by these patterns into the optical waveguide modes of the absorber layer. Further optimization of the height of the structures should be performed in order to find optimum light trapping, in which the diffraction is strong enough, as discussed in section 3.3, while making sure that the waveguide modes are not significantly perturbed by the presence of these scatterers.

Besides this further optimization, we can also take a more theoretical approach to study the limit for light trapping in an absorbing thin film with optimized nanostructures. For poorly-absorbing thick solar cells with a random texture we can use ray optics to predict a maximum path length enhancement of $4n^2$, with n being the refractive index of the material, as derived by Yablonovitch [28, 29]. In our case, in which the films are thin and highly absorbing, we should consider the exact criteria that determine the excitation of the modes. Apart from the wavevector matching, other factors, such as the overlap of the scattered electric and magnetic fields with the ones from the waveguide modes, also play a role in determining the coupling efficiency, and thus, the limit for light trapping [30]. This coupling efficiency could be calculated with RETOP, a near-to-far-field transformation (NFFT) open software that allows to obtain the far field of light scattered by a nanopattern inside a layered structure [31]. However, the model does not account for absorbing media, such as photovoltaic materials, and therefore can only be used as a first approach.

Chapter 5

CATHODOLUMINESCENCE SPECTROSCOPY ON CZTS

Finally, we devote the last chapter to consider a different approach towards the study of thin film PV materials and, in particular, CZTS. Even though light trapping strategies can improve the absorption of CZTS solar cells, their efficiencies are still far from their Shockley-Queisser limits. We can address this issue by studying the material properties through CL spectroscopy. In particular, we will start a first approach to study the band gap energy of the material, together with possible variations at different positions and depths.

5.1 Introduction to CL spectroscopy

When an electron beam, with energy ranging from 1 to 30 keV, interacts with a material, several processes can take place. The generation of secondary and backscattered electrons (SE and BSE, respectively) are two examples of these mechanisms, which allows us to obtain information about the surface of the samples. In addition to this, electromagnetic radiation from a broad spectral range can also be generated. Several techniques rely on the detection of this radiation, such as energy-dispersive X-ray spectroscopy (EDS), which detects the emitted X-rays and allows for the chemical characterization of the sample, and cathodoluminescence (CL), which studies the light emitted in the visible and near-infrared spectral range, therefore allowing us to probe the band gap of semiconductors, among others. A schematic of our CL setup (Delmic SPARC) is shown in fig. 5.1, which consists of a modified SEM (QUANTA FEG 650) containing a parabolic mirror. Light emitted by the sample is collected by the mirror, coupled with a lens into a fiber and sent to a spectrometer (SpectraPro 2300i) [32, 33].

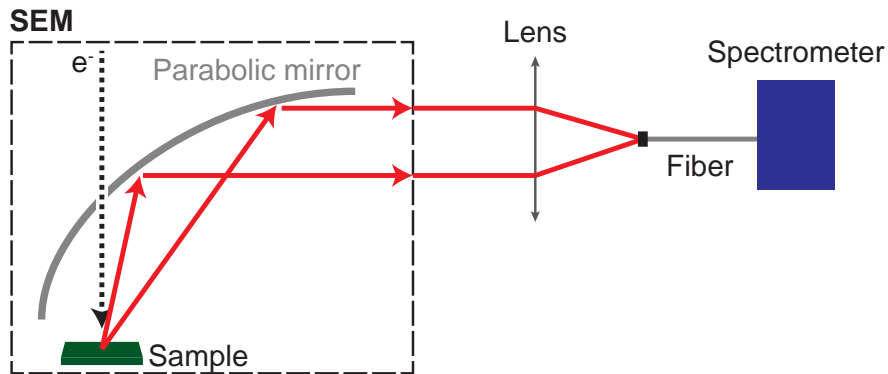


Figure 5.1: **Schematic of the cathodoluminescence spectroscopy setup.** The setup is based on a modified SEM with a parabolic mirror placed above the sample, which allows to collect the emitted light. The latter is then coupled into a fiber and sent to a spectrometer, thus allowing us to obtain the spectrum of the light emitted at each position on the sample.

5.2 Energy-dependence of the penetration depth of e^-

We want to analyse a CZTS layer, contained in a multilayer structure similar to the one of the solar cell from the previous chapter. However, in this case we only have CdS on top, therefore the electrons can penetrate towards the CZTS, as will be discussed. The geometry of our sample is depicted in 5.2 (a), with indicative values for the thickness of each layer that have been extracted from the cross section shown in 5.2 (b). In addition to these layers, we could also expect to have a thin film of MoS_x at the interface between Mo and CZTS that is formed during the synthesis of the material [34]. Figure 5.2 (c) shows an SEM top view image of the sample. In both SEM images we can observe that the CZTS layer is inhomogeneous in height, with thickness ranging from 600 to 1 μm . Moreover, there are some bright particles on the surface, which correspond to clusters of CdS, according to EDX measurements.

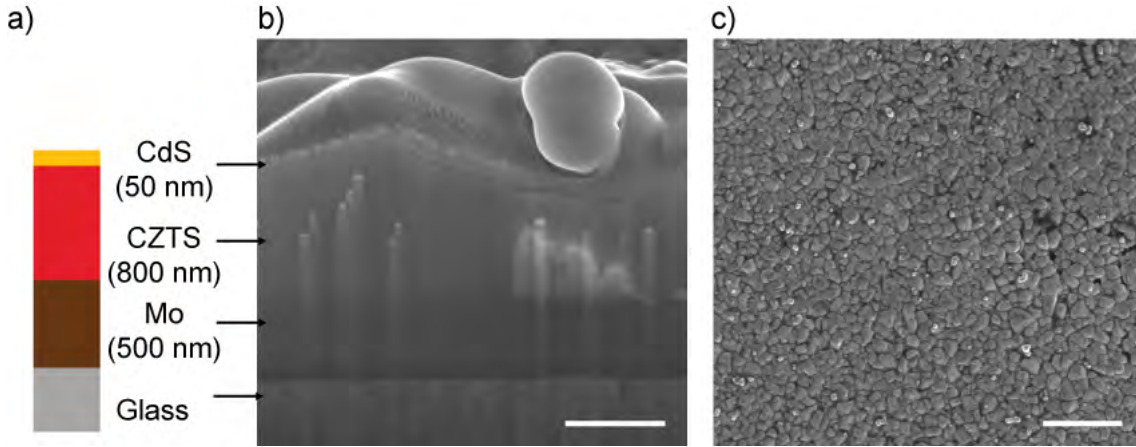


Figure 5.2: **Multilayer sample containing CZTS.** (a) Geometry of the sample. The value of thickness is indicative and has been determined from the cross section in (b). (b) SEM image of a cross section performed with FIB, from which we can see that the layer of CZTS is not homogeneous in thickness. The scale indicates 500 nm. (c) Top view image of the sample, showing the CdS layer. In this case the scale equals to 1 μm .

Given that we have a multilayer structure, it is important to consider the initial energy of the electrons, which will determine the penetration depth into the sample. We can evaluate the energy at which electrons will reach each point of the material by using Casino, a Monte Carlo based software [35]. Figure 5.3 shows the trajectories of the electrons inside the material, for incoming energy of 5, 10 and 30 keV (a, b and c, respectively). Each dot in the figure represents a collision of an electron with the material and the energy after this interaction is represented through the colour scale, relative to the initial energy. We observe that when the electron beam has an initial energy of 5 keV, electrons mainly probe the CdS layer and reach the CZTS with low energy, thus we expect to receive light mostly from CdS. Instead, at 10 keV, electrons reach the CZTS with relatively high energy, therefore we are probing both CdS and CZTS. Finally, at 30 keV the entire sample up to Mo is reached with relatively high energy electrons.

Taking the simulations into account, we can now look at the spectra of the light collected

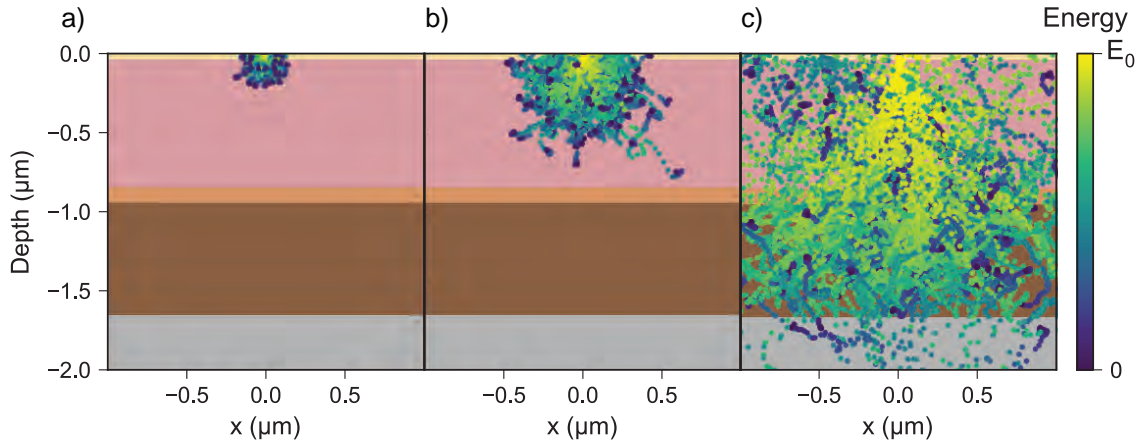


Figure 5.3: **Penetration depth of electrons inside the sample.** Simulations for initial electron energies of (a) 5 keV, (b) 10 keV and (c) 30 keV. Each dot represents a collision of the electrons with the material, and the colour scale determines the energy with respect to the initial one. The simulations have been performed using a Monte Carlo-based software (Casino).

for different electron beam energies. Figure 5.4 shows the typical spectra obtained at 5, 10 and 30 keV (blue, green and red, respectively), with the vertical axis corresponding to the normalized CL intensity. In order to cover the complete visible spectral range, we need to perform two measurements, each of them with a different grating to disperse the light on the detector. Therefore, the information is split into two plots, corresponding to short (a) and large (b) wavelength range. If we first focus on the measurements at 5 keV (blue curves), we can identify three main peaks over the entire visible spectrum. The first one, at 510 nm, matches with the band gap of CdS, expected to be around 504 nm (2.46 eV) [36]. The second and third peaks correspond to wavelengths of 760 and 910 nm, which do not match directly with the band gap of CZTS, expected to be around 825 nm (1.5 eV) [26]. If we now analyse the spectra obtained for initial electron energy of 10 keV (green curve), we see that the peak at 510 nm decreases. Given that we know that at this energies most of our signal will come from the CZTS, this observation suggests that indeed the peak corresponds to CdS. In addition to this, the peak at 760 nm becomes practically negligible, thus meaning that it is probably related either to CdS or to the surface of CZTS. Instead, the peak at 920 nm, which is now slightly shifted due to the fact that there is not another peak nearby, becomes clearer, indicating that it might come from CZTS. This assumption is supported by the spectrum at 30 keV (red curve), in which we can only appreciate the peak at 920 nm. The spectrum in the short wavelength range did not exhibit any clear feature but noise.

5.3 Large area integrated intensity map

We first performed a scan of a large area (a few micrometers), as shown in fig. 5.5, and collected both the secondary electrons (a) and the total emitted light (b) at each position. In this case we used a photomultiplier tube (Hamamatsu Photonics) enhanced in the near infrared instead of a spectrometer, thus we cannot distinguish among light emitted at different wavelengths. We used an electron beam energy of 5 keV, meaning that we were mainly probing CdS and the most superficial layer of CZTS. When analysing the CL

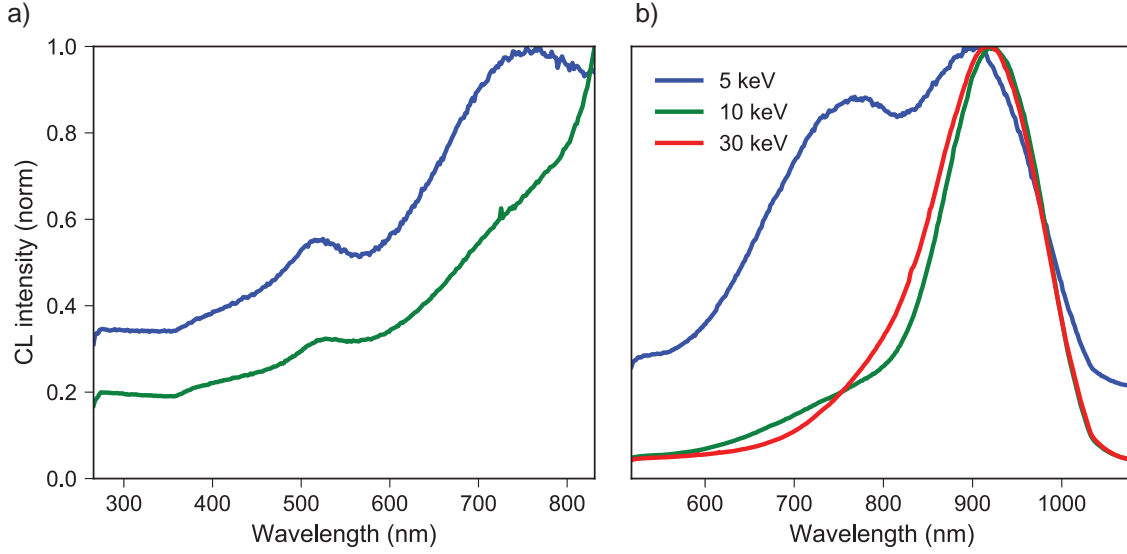


Figure 5.4: CL spectra for different energies of the incoming electron beam. (a) Normalized CL intensity as a function of the wavelength in the range from 300 to 800 nm, for electron beam energies of 5 and 10 keV (blue and green). (b) Same plot but in a wavelength range from 500 to 1100 nm, now for electron beam energies of 5, 10 and 30 keV (red). The 5 keV exhibits a peak at 510 nm, matching with the band gap of CdS, in addition of two peaks at 760 and 910 nm. In the spectra for larger energies, the first and second peak become practically negligible, while the third one is now slight shifted towards 920 nm due to the absence of the rest of peaks. The presence of this peak at high energies suggests that it comes from the CZTS layer.

intensity map, we should first notice that the emission is quite uniform over the entire sample, as can be seen from the colour scale. Nevertheless, if we consider the relative values among different positions, we can identify a relation between the emission of light and the morphology of the surface. This can imply either that the emission is directly related to variations in the sample, such as grain boundaries or difference in thickness, or that the emission is the same but the collection efficiency depends on the morphology. In addition to this, we can also observe that the CdS particles exhibit a higher CL emission relative to the rest of the sample.

5.4 CL spectra at different positions

We can now perform further measurements to study in depth the peaks shown in the spectra from fig. 5.4. We used an electron beam energy of 10 keV, since it allows to probe the CZTS while still obtaining some information from either CdS or the most superficial part of the CZTS layer. We performed six different measurements at several regions on our sample, with separations among them ranging from 20 μm to 2 mm. In each measurement the electron beam scans a certain area, with typical size 1 μm^2 , thus collecting both the secondary electrons and the CL emission at each scanning step.

All of the regions that we measured exhibited similar spectral features, as discussed in appendix C.1, therefore in the following we will focus on one of them, which can be

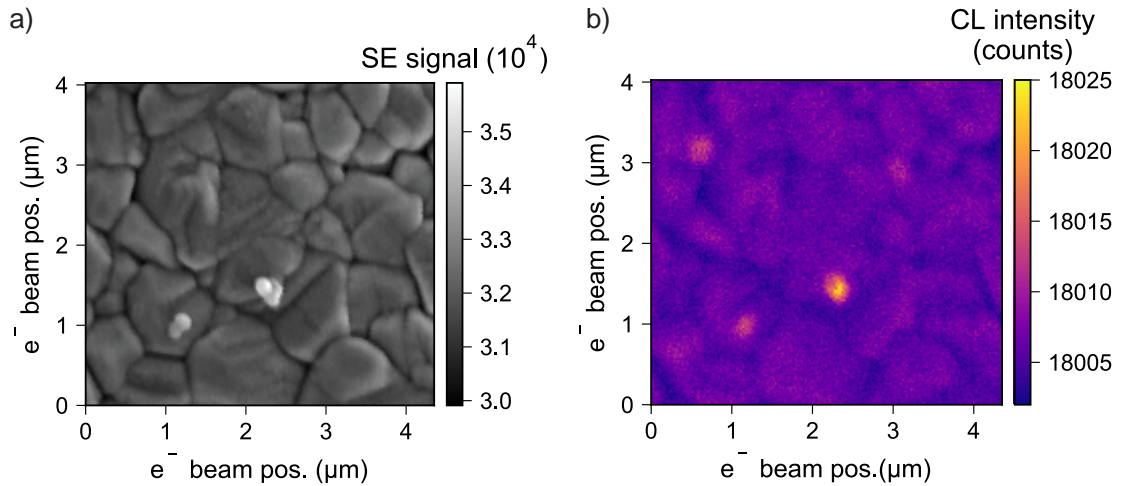


Figure 5.5: **Large integrated intensity map at 5 keV.** (a) SEM image and (b) CL intensity map of a 4x4 μm² area of the sample. The colour scale of the collected CL intensity shows that the emission is quite homogeneous over the entire region. However, there exist relative difference in the amount of light emitted related to the morphology of the sample.

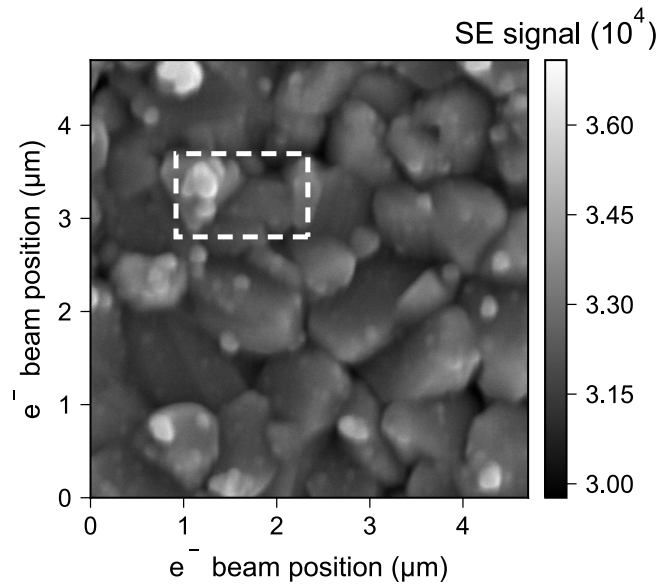


Figure 5.6: **Top view SEM image of the region of the sample under study.** The rectangle indicates the exact area in which the scanning is performed, thus collection both secondary electrons and CL emission.

considered as a typical example. Figure 5.6 shows the SEM image of the region that we will discuss, where the rectangle indicates the exact area in which the scan was performed. In particular, we extracted the CL spectrum at three characteristic locations on the sample: on top of a CdS particle, on the CdS layer and on what appears to be a grain boundary. The spectra of these positions, together with the corresponding SEM image can be seen in 5.7. We can observe that the spectrum from the CdS particle (orange curve) is the only one that exhibits peaks at 520 and 760 nm, in addition to the one at 920 nm, thus suggesting

again that they come from this material and not CZTS. Furthermore, in the three cases there is a strong peak around 920 nm. Notice that the peak from the CdS particle looks slightly blue shifted, but it is only an effect of being close to another peak, as discussed in C.2. The intensity of this peak is higher for the position at the grain boundary (purple), which agrees with the idea that it comes from CZTS.

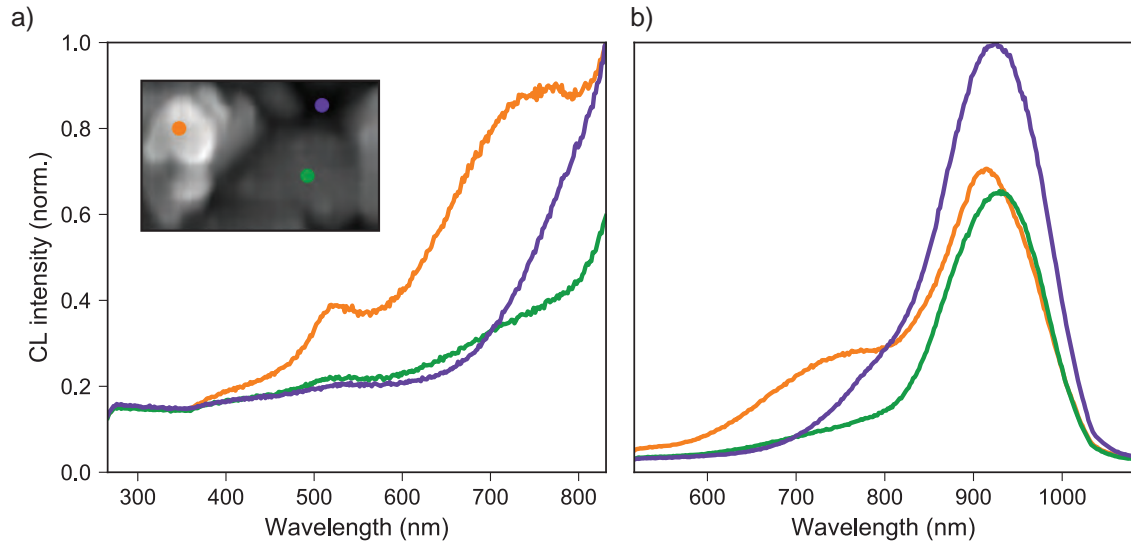


Figure 5.7: CL spectra at characteristic locations of the sample. Normalized CL intensity for short (a) and long (b) wavelengths obtained at the three positions indicated in the SEM image in (a), corresponding to a CdS particle (orange), the CdS layer (green) and a grain boundary-like location, where the layer of CZTS is probably thinner (c). The colour of each curve corresponds to the dots on the image, thus indicating the exact positions that were excited by the electron beam. The peaks at 520 and 760 nm are mostly present in the spectrum from the CdS particle, thus suggesting a correlation with the presence of CdS. Instead, the peak at 920 nm is exhibited in all the spectra but becomes more significant at the second and third positions, which agrees with the fact that it can be related to CZTS.

During the data acquisition we can also obtain CL intensity maps at the desired wavelengths and bandwidth, which we can use as a further proof for the relation of the peaks with the different materials. Figure 5.8 shows the maps at 520, 760 and 920 nm (b-c), with a spectral bandwidth of 50 nm, together with the corresponding SEM image (a). Since the maps at 760 and 920 nm are obtained from the same acquisition, we can compare the intensity between both and therefore they have the same normalization factor. The maps at 520 and 760 nm exhibit a similar behaviour, with the CdS being the most intense spot compared to the rest of the region, agreeing again with the strong correlation of these peaks with the presence CdS. In contrast, the map centred at 920 nm exhibits an almost opposite behaviour, with most of the light coming from the grain boundary-like position. Moreover, the intensity in this map is higher than for the 720 nm, therefore meaning that the contribution of the latter is small.

Taking these measurements into account, we can conclude that the peaks at 520 and 760 nm are related to the presence of CdS. However, while the first one matches perfectly with the

band gap of this material, the second one does not have a direct link. A possible origin of this peak could be the presence of defect states in CdS, which have been shown to emit light in a wavelength range close to 760 nm [32]. Additionally, we could also think that this peak is related to the surface of the CZTS or even the interface between the latter and CdS. Some studies suggest that the stannite phase of CZTS has a band gap energy close to 1.3 eV, in contrast to the usual kesterite with a band gap at 1.5 eV [25, 37, 38]. However, this would not explain the correlation that we see with the CdS layer, unless there was a relation between CdS and the presence of a particular phase of CZTS. Finally, we can also conclude that the peak at 920 nm corresponds to CZTS, even though it does not match with the expected band gap (~ 825 nm). Previous works on photoluminescence (PL) have reported a similar shift between the PL intensity peak and the actual band gap derived from the absorption coefficient spectrum [39, 40]. These differences were suggested to be due to band to impurity radiative recombination or inhomogeneities in the CZTS layer, which in our case is less probably since we have measured several regions, all of them with the same results (C.1)

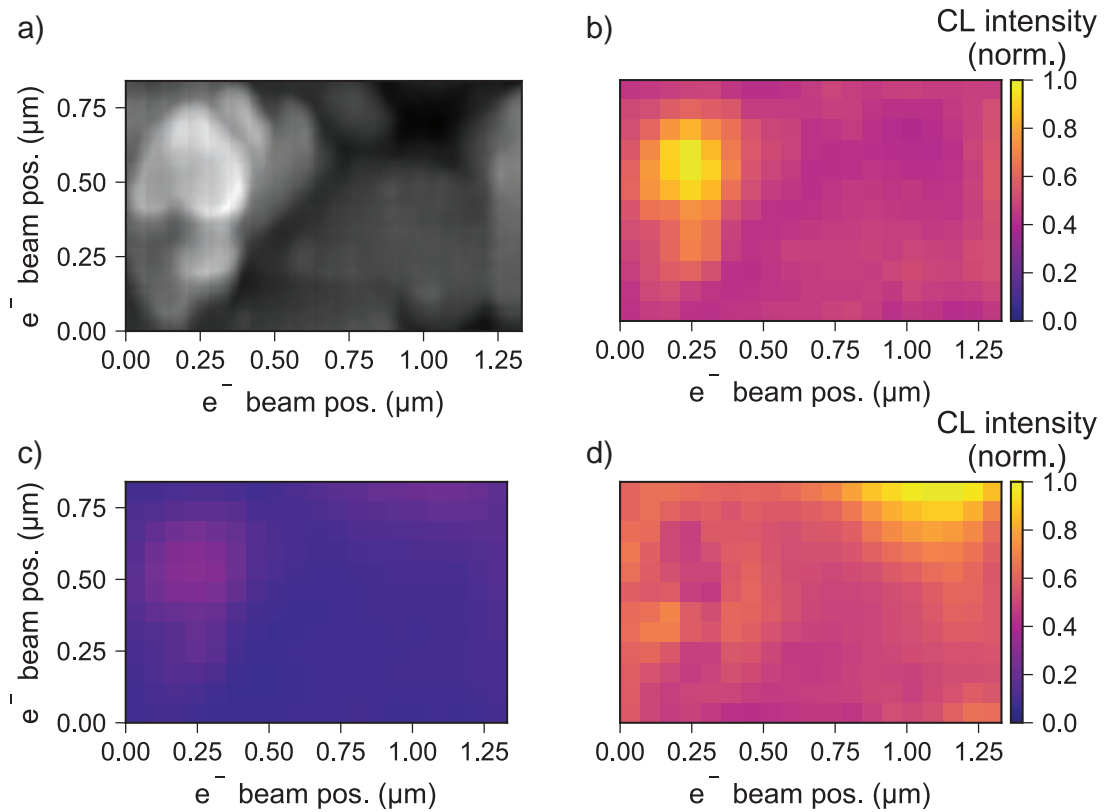


Figure 5.8: CL intensity maps for different central wavelengths. (a) SEM image of the region, together with the CL intensity map with central wavelength at 520, 720 and 960 nm (b, c and d, respectively), all of them with a spectral bandwidth of 50 nm. Again, the maps at 520 and 760 nm exhibit a similar intensity distribution, with the highest emission coming from the CdS particle. Instead, the map at 920 nm shows a higher emission in the grain boundary-like area.

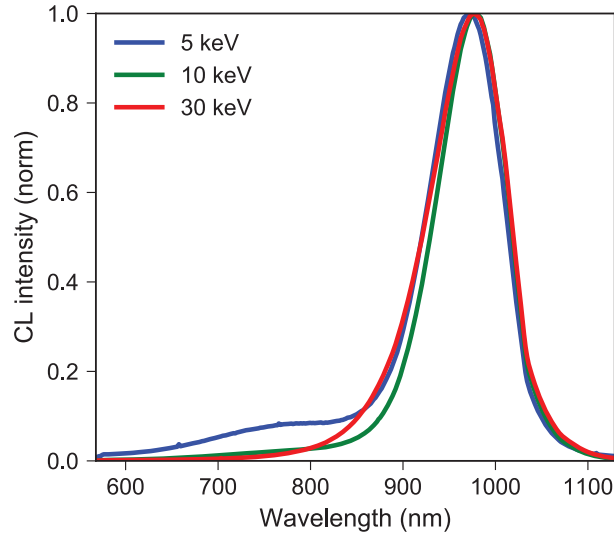


Figure 5.9: **CL intensity spectra for different energies of the incoming electron beam at low temperatures.** The three spectra, corresponding to electron beam energies of 5, 10 and 30 keV (blue, green and red, respectively) exhibit a main peak around 970 nm, which is red shifted with respect to the previous measurements at ambient temperature. Moreover, the peak at 760 nm is almost negligible now and we can only appreciate a small tail towards 700 nm for the lowest beam energy.

5.5 CL spectroscopy at low temperature

Finally, we also performed CL measurements at low temperatures, which can be achieved by using a cryostage that cools the sample holder, and therefore the sample, thanks to a flux of cold N_2 vapour. The temperature of the sample should be around $-190^\circ C$, but cannot be determined precisely since we can only measure the temperature of the holder. The CL emission can be generally modelled as a Gaussian, as done in appendix C.2, with the broadening being determined by the distribution of the available energy, due to the coupling with phonon bath. Since the latter is strongly dependent on the temperature, we expect to observe narrower emission peaks at low temperatures [41], which might allows us to identify and characterize more easily the main peaks in the spectrum, together with possible variations over position or depth. Figure 5.9 shows the CL intensity spectrum at long wavelengths for the three beam energies discussed in section 5.2: 5, 10 and 30 keV. The spectra at short wavelengths are not shown since they did not exhibit any clear feature. We can observe that in this case the three spectra are very similar among them, with a main peak at 975 nm. Only the curve from the lowest beam energy exhibits a small tail towards shorter wavelengths, until around 700 nm, probably corresponding to the broad peak around 720 nm observed in the previous measurements. This behaviour was seen in all the measured samples, as shown in fig. C.2 from the appendix.

Taking into account these results, we can observe that decreasing the temperature of the sample leads to two main differences with respect to the room temperature measurements. The first one is a red shift of the main peak, which is now centred at 975 nm (1.27 eV), in contrast to the previous 920 nm (1.35 eV). Since the band gap of a semiconductor is

expected to increase with decreasing temperatures [42, 43], in contrast to what we observe, this result supports the hypothesis that the origin of this CL peak is not directly related to the band gap but accounts for other luminescent processes. Moreover, the same effect has also been observed in previous works on photoluminescence [44], even though there is still discussion regarding this temperature dependence [34]. The second effect observed is that the intensity of the peak at 760 nm becomes very small compared to the one at 975 nm. This could mean either that the source of this peak is less luminescent at low temperatures or that the other peak at larger wavelength increases more compared to this one. Possible hypotheses for this phenomenon could be that the emission of defect states of CdS that might originate this peak decreases at low temperature or that changes in temperature induce variations in the structural phase in CZTS, which is usually kesterite at room temperature, and therefore changes in the emission spectra. In any case, further assessment of these results needs to be done, which goes beyond the scope of this thesis, in order to fully understand the different defect states and emission mechanisms inside this material.

Chapter 6

CONCLUSIONS AND OUTLOOK

In this thesis we have focused on improving the performance of ultrathin solar cells, with a particular focus on $\text{Cu}_2\text{ZnSnS}_4$ (CZTS) and $\text{CuIn}_x\text{Ga}_{1-x}\text{Se}_2$ (CIGSe), by adding dielectric nanopatterns that allow for light coupling into the optical waveguide modes of the absorber layer. In particular, we have fabricated arrays of nanoparticles with different distributions (periodic, random and optimized) with substrate conformal lithography (SCIL), and optimized textures, referred to as zebra patterns, with focused ion beam (FIB) milling and electron beam lithography (e-beam). Next, the power spectral density (PSD) of these samples has been measured by means of a home-built Fourier microscope, with the results showing that both the optimized array of nanoparticles and especially the zebra patterns scatter light mainly within a designed range of momenta $k_{||}$. This range can be tailored to match the wavevectors of the waveguide modes and, therefore, enabling the coupling of light within a broad range of wavelengths.

We have also analysed the excitation of waveguide modes due to the presence of dielectric nanopatterns through two different examples. The absorption enhancement in periodically-patterned CIGSe solar cells has been analysed by calculating the dispersion relations of the absorber layer and relating the peaks observed in the experimental results to the coupling of light scattered by the grating into the modes. We have also analysed the effect of zebra patterns in 400 nm-thick CZTS solar cells by means of FDTD simulations. The results show that the overall absorption is increased with respect to the unpatterned cell, especially at long wavelengths, leading to a predicted 6 % rise in the short current density of the patterned cell.

In order to fully elucidate the excitation mechanisms and efficiency of light coupling to waveguide modes further research is needed. A next step would be the optimization of not only the shape of the nanopatterns, as we have done, but also the height and material used for the patterns inside the solar cells. Furthermore, we should investigate the exact criteria required for coupling to waveguide modes, since we know that other factors apart from wavevector matching, such as the profile of the electric and magnetic fields, can play an important role. This study could allow us to obtain a theoretical maximum for light trapping in patterned thin film cells, analogue to the $4n^2$ light trapping limit for randomly textured layers.

Finally, we have investigated the optical properties of CZTS by means of cathodoluminescence (CL) spectroscopy. As a first result, we have observed that the CL spectra do not exhibit significant variations over different regions and depths on the sample. Specifically, the spectra show three main luminescent peaks at 520, 760 and 920 nm. Our study suggests that the first peak is due to emission from the thin CdS layer on top of the CZTS, while the origin of the second one still remains unclear, since it could be either from the CdS or

the CdS/CZTS interface. Instead, the peak at 920 nm probably comes from CZTS, even though it does not match with the band gap extracted from the literature, meaning that it is probably due to the presence of other radiative channels. In any case, the results of CL on this sample are still preliminary and further research needs to be assessed in order to fully understand the different luminescent emission processes.

Part of this thesis has been published in the following paper:

Yin, G., Knight, M., van Lare, M, Solà Garcia, M. M., Polman, A. & Schmid, M. Optoelectronic Enhancement of Ultrathin $\text{CuIn}_{1-x}\text{G}_x\text{Se}_2$ Solar Cells by Nanophotonic Contacts. *Advanced Optical Materials*, **5**(5), 1600637 (2016).

Particularly, the dispersion relations for the CIGSe solar cell geometry in the paper and the electric field distributions of the modes have been calculated by M. Magdalena Solà Garcia.

BIBLIOGRAPHY

1. National renewable energy laboratory (NREL). *Best research-cell efficiencies*. <https://www.nrel.gov/pv/assets/images/efficiency-chart.png> (2017).
2. Fraunhofer Institute for Solar Energy Systems. *Photovoltaics report* <https://www.ise.fraunhofer.de> (2016).
3. Open Energy Information. *Transparent cost database*. <http://en.openei.org/apps/TCDB/> (2017).
4. Palik, E. *Handbook of Optical Constants of Solids: Index* **225**, 559–578 (Academic Press, 1998).
5. Yin, G. *et al.* Optoelectronic Enhancement of Ultrathin $\text{CuIn}_{1-x}\text{Ga}_x\text{Se}_2$ Solar Cells by Nanophotonic Contacts. *Advanced Optical Materials* **5**, 1600637 (2016).
6. Van Lare, M. C. & Polman, A. Optimized Scattering Power Spectral Density of Photovoltaic Light-Trapping Patterns. *ACS Photonics* **2**, 822–831 (2015).
7. Paetzold, U. W., Lehnen, S., Bittkau, K., Rau, U. & Carius, R. Nanoscale observation of waveguide modes enhancing the efficiency of solar cells. *Nano Letters* **14**, 6599–6605 (2014).
8. Van Lare, C., Yin, G., Polman, A. & Schmid, M. Light Coupling and Trapping in Ultrathin $\text{Cu}(\text{In,Ga})\text{Se}_2$ Solar Cells Using Dielectric Scattering Patterns. *ACS Nano* **9**, 9603–9613 (2015).
9. Ferry, V. E. *et al.* Light trapping in ultrathin plasmonic solar cells. *Opt. Express* **18**, 237–245 (2010).
10. Sersic, I., Tuambilangana, C. & Koenderink, A. F. Fourier microscopy of single plasmonic scatterers. *New Journal of Physics* **13**, 083019 (2011).
11. Kurvits, J. A., Jiang, M. & Zia, R. Comparative analysis of imaging configurations and objectives for Fourier microscopy. *Journal of the Optical Society of America A* **32**, 2082 (2015).
12. Verschuuren, M. *Substrate Conformal Imprint Lithography for Nanophotonics*. (2009).
13. Library, S. P. *Fourier transforms* <https://docs.scipy.org/doc/scipy/reference/fftpack.html> (2017).
14. Battaglia, C. *et al.* Light Trapping in Solar Cells : Can Periodic Beat Random? *ACS Nano*, 2790–2797 (2012).
15. Wuttke, J. Form factor (Fourier shape transform) of polygon and polyhedron. *ArXiv*, 1–15 (2017).
16. Born, M. & Wolf, E. *Principles of optics* (1999).
17. Palmer, C. & Loewen, E. *Diffraction grating handbook* (New York: Newport Corporation, 2005).

18. Silfvast, W. T. *Laser fundamentals* (Cambridge University Press, 2004).
19. Divitt, S. & Novotny, L. Spatial coherence of sunlight and its implications for light management in photovoltaics. *Optica* **2**, 95 (2015).
20. Green, M. A. *et al.* Solar cell efficiency tables (version 49). *Prog. Photovolt: Res. Appl.* **25**, 3–13 (2017).
21. Jackson, P. *et al.* Properties of Cu(In,Ga)Se₂ solar cells with new record efficiencies up to 21.7%. *physica status solidi (RRL) – Rapid Research Letters* **9**, 28–31 (2015).
22. Lumerical Solutions, Inc <http://www.lumerical.com/tcad-products/fdtd/>.
23. Verhagen, E. *Subwavelength light confinement with surface plasmon polaritons* (2009).
24. Van de Groep, J. *Light trapping in thin silicon waveguides by plasmon mediated mode coupling* (2011).
25. Botti, S., Kammerlander, D. & Marques, M. A. L. Band structures of Cu₂ZnSnS₄ and Cu₂ZnSnSe₄ from many-body methods. *Applied Physics Letters* **98**, 4–7 (2011).
26. Sun, K. *et al.* Over 9% Efficient Kesterite Cu₂ZnSnS₄ Solar Cell Fabricated by Using Zn_{1-x}Cd_xS Buffer Layer. *Advanced Energy Materials* **6**, 4–9 (2016).
27. Li, S. Y. *et al.* Optical properties of reactively sputtered Cu₂ZnSnS₄ solar absorbers determined by spectroscopic ellipsometry and spectrophotometry. *Solar Energy Materials and Solar Cells* **149**, 170–178 (2016).
28. Yablonovitch, E. Statistical ray optics. *Journal of the Optical Society of America* **72**, 899 (1982).
29. Yablonovitch, E & Cody, G. D. Intensity Enhancement in Textured Optical Sheets for Solar-Cells. *IEEE Transactions on Electron Devices* **29**, 300–305 (1982).
30. Beck, F. J., Stavrinadis, A., Lasanta, T., Szczepanick, J.-P. & Konstantatos, G. Understanding light trapping by resonant coupling to guided modes and the importance of the mode profile. *Optics Express* **24**, 759 (2016).
31. Yang, J., Hugonin, J. P. & Lalanne, P. Near-to-Far Field Transformations for Radiative and Guided Waves. *ACS Photonics* **3**, 395–402 (2016).
32. Coenen, T. *Angle-resolved cathodoluminescence nanoscopy* (2014).
33. Brenny, B. J. M. *Probing Light Emission At the Nanoscale With* (2016).
34. Liu, X. *et al.* The current status and future prospects of kesterite solar cells: a brief review. *Progress in photovoltaics* **24**, 879–898 (2016).
35. Drouin, D. *et al.* CASINO V2.42 - A fast and easy-to-use modeling tool for scanning electron microscopy and microanalysis users. *Scanning* **29**, 92–101 (2007).
36. Boakye, F. & Nusenu, D. The energy band gap of cadmium sulphide. *Solid State Communications* **102**, 323–326 (1997).
37. Shibuya, T. *et al.* From kesterite to stannite photovoltaics: Stability and band gaps of the Cu₂(Zn,Fe)SnS₄ alloy. *Applied Physics Letters* **104**, 3–6 (2014).

38. Zhao, Z. & Zhao, X. Electronic, optical, and mechanical properties of $\text{Cu}_2\text{ZnSnS}_4$ with four crystal structures. *Journal of Semiconductors* **36**, 083004 (2015).
39. Todorov, T. K. *et al.* Beyond 11% Efficiency: Characteristics of State-of-the-Art $\text{Cu}_2\text{ZnSn}(\text{S},\text{Se})_4$ Solar Cells. *Advanced Energy Materials* **3**, 34–38 (2013).
40. Dhakal, T. P., Peng, C. Y., Reid Tobias, R., Dasharathy, R. & Westgate, C. R. Characterization of a CZTS thin film solar cell grown by sputtering method. *Solar Energy* **100**, 23–30 (2014).
41. Suyver, J. F., Kelly, J. J. & Meijerink, A. Temperature-induced line broadening, line narrowing and line shift in the luminescence of nanocrystalline ZnS:Mn^{2+} . *Journal of Luminescence* **104**, 187–196. ISSN: 00222313 (2003).
42. O'Donnell, K. P. & Chen, X. Temperature dependence of semiconductor band gaps. *Applied Physics Letters* **58**, 2924–2926 (1991).
43. Sarswat, P. K. & Free, M. L. A study of energy band gap versus temperature for $\text{Cu}_2\text{ZnSnS}_4$ thin films. *Physica B: Condensed Matter* **407**, 108–111 (2012).
44. Tanaka, K., Miyamoto, Y., Uchiki, H., Nakazawa, K. & Araki, H. Donor-acceptor pair recombination luminescence from $\text{Cu}_2\text{ZnSnS}_4$ bulk single crystals. *Physica Status Solidi (A) Applications and Materials Science* **203**, 2891–2896 (2006).
45. Crovetto, A., Cazzaniga, A., Ettlinger, R. B., Schou, J. & Hansen, O. Optical properties and surface characterization of pulsed laser-deposited $\text{Cu}_2\text{ZnSnS}_4$ by spectroscopic ellipsometry. *Thin Solid Films* **582**, 203–207 (2015).
46. Princeton Instruments. *SpectraPro 2300 Series*

ACKNOWLEDGEMENTS

The results of this Master's thesis and all the knowledge that I have acquired during this year at AMOLF could not have been possible without the help and support of a lot of people, to whom I want to show my sincere gratitude. First of all, thanks to Albert Polman for allowing me to perform my research in his group and, with this, letting me discover and be even more fascinated by the world of nanophotonics, photovoltaics and, of course, cathodoluminescence. Moreover, I really appreciate his always motivating *coaching* and the generous opportunities that offers to all of his students, which have allowed me to grow both from a scientific and personal perspective. In addition to Albert, I want to thank Tom Gregorkiewicz for being my second examiner and taking time to correct this thesis.

Verena Neder has been a key person in the development of this thesis. I cannot thank her enough for all the help and support that she has continuously given to me. She always had time to discuss even the smallest details about my project and her eagerness to always understand and question things has always inspired me to improve my research. Moreover, she is an excellent office mate, with whom to always laugh -and share food. Mark Knight also played an important role while he was at AMOLF: I want to thank him for his always useful scientific advice, his will to help with any problem and for teaching me some of his perfectionism. Next, Sophie Meuret deserves a special mention, for always being there to discuss and offer another point of view, and for her infinite enthusiasm. And equally to the previous mentioned people, I want to express my gratitude to Tom Veecken, Nick Schilder, Andrea Cordaro, Toon Coenen and Cyrian Leriche for their support, useful discussions and good moments. It is a pleasure to be part of this group.

Apart from the members of my group, there have been many other people that have helped me during this research. I want to thank Dimitry Lamers, Bob Drent, Andries Lof and Hans Zeijlemaker for their help and discussions during the fabrication of my structures. The fabrication of the zebra patterns would have never been possible without you! In a similar way, I want to express my gratitude to Cocoa Guo, Femius Koenderink, Wouter den Hollander and Marko Kamp for always being available to patiently answer all of my questions during my immersion into Fourier microscopy.

Last but not least, I would like to thank my family for their countless support and for always encouraging me to pursue what I want. And of course, a special thanks is for Noel, for always being there.

Appendix A

ADDITIONAL CHARACTERIZATION OF FOURIER MICROSCOPE

A.1 Measurements at 490 nm

The Fourier microscopy measurements and characterization were also performed for an illumination with a wavelength 490 nm as a further test for the microscope. The correction function is shown in fig. A.1 and the measurements of the nanoparticle arrays and zebra patterns can be seen in A.2 and A.3. Now the maximum $k_{||}$ that we can collect is $17.9 \text{ rad } \mu\text{m}^{-1}$. All the measurements exhibit the same trends as before. In particular, the comparison between the random and optimized arrays (A.2, b-c) becomes clearer, since for the optimized array we can observe a more defined ring at the limits of the BFP.

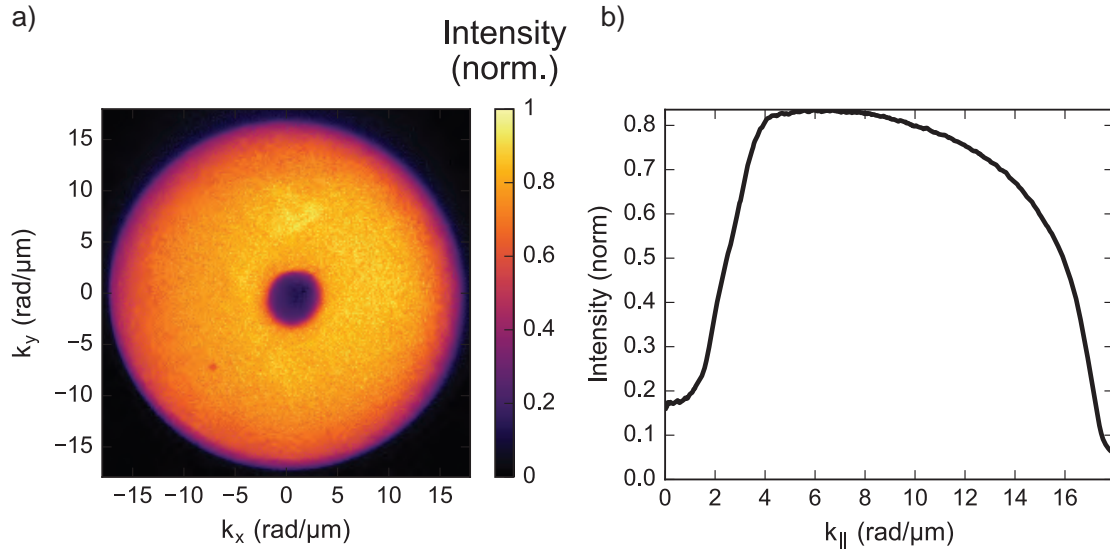


Figure A.1: **Correction function for illumination at $\lambda=490 \text{ nm}$.** (a) Fourier image and (b) integrated intensity over the angle of the correction function that needs to be applied to all of the measurements.

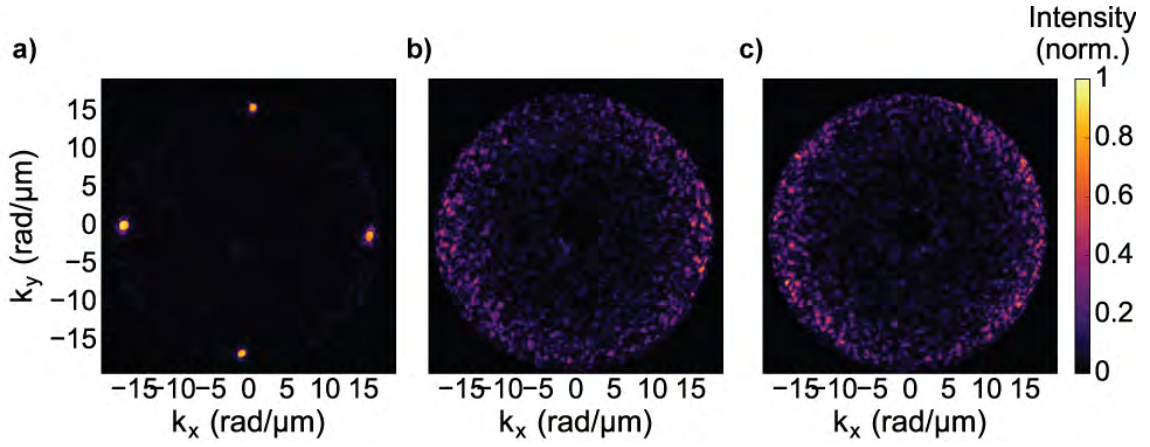


Figure A.2: **Fourier microscopy measurements of arrays of nanoparticles with illumination at $\lambda=490$ nm.** Fourier images of (a) periodic, (b) random and (c) optimized arrays of nanoparticles. The illumination was now with a wavelength of 490 nm and therefore the maximum $k_{||}$ that can be collected is smaller than for the previous measurements at 405 nm. The results show the same trends as for the previous measurements at $\lambda=405$ nm. The comparison between the random and optimized arrays shows that the latter exhibits a clearer ring at the limits of $k_{||}$, as expected from the discrete Fourier transforms.

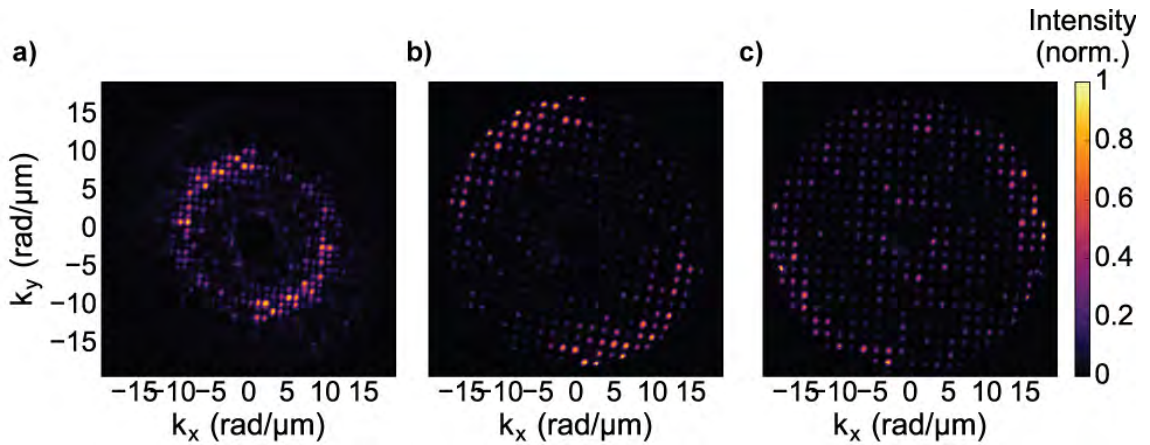


Figure A.3: **Fourier microscopy measurements of zebra patterns with illumination at $\lambda=490$ nm.** Fourier images of zebra patterns fabricated with FIB (a,b) and e-beam (c). The fields have unit cells of $6.5 \times 6.5 \mu\text{m}^2$ (a) and $4 \times 4 \mu\text{m}^2$ (b, c). The illumination was now with a wavelength of 490 nm. The results show the same trends as for the previous measurements at $\lambda=405$ nm.

A.2 Dye experiment to obtain NA

A schematic of the measurement performed with a fluorescent dye is shown in fig A.4. A fluorescent dye (absorbing at wavelength $\lambda_{abs} \approx 405$ nm and emitting at $\lambda_{em} \approx 650$ nm) is spin coated on a glass slide. In this case, the dye is facing downwards having air below, while the glass faces the immersion oil. When light excites the fluorescent molecules, we can consider that they will emit isotropically. Light emitted downwards at small angles will be transmitted towards the air and, therefore, will not be captured by the objective. However, light emitted at high angles will suffer total internal reflection and, since the refractive index of the glass is very similar to the one for the oil, will be transmitted towards both materials and be captured by the objective. Therefore, if we now recall the relation between the momentum of light and its angle (eq. 2.1), we know that we will collect only half of the light emitted with a momentum $k_{||} < k_0 n_{air} = k_0$, since the other half escapes to the air, and all the light emitted with $k_0 < k_{||} < k_{max}$. Therefore, we expect to see an increase in intensity between $k_{||} = k_0$ and $k_{max} = k_{||} = NA k_0$.

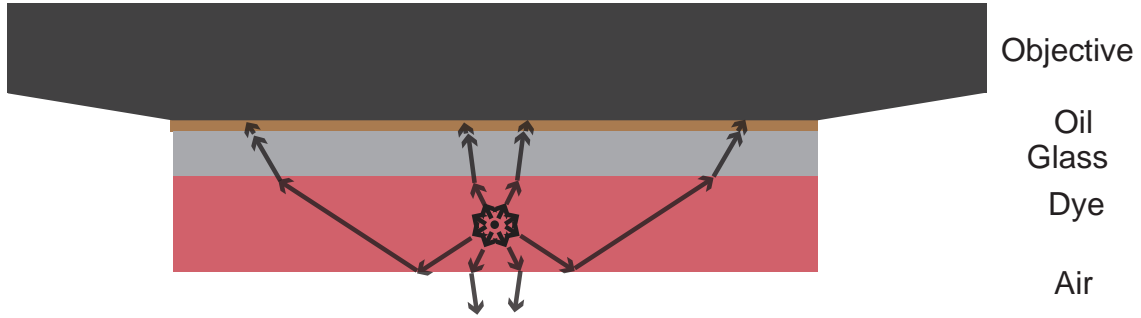


Figure A.4: **Schematic of the emission of a dye.** We consider that light is emitted isotropically in the dye. Therefore, light that is emitted downwards with $k_{||} < k_0$ will be able to escape towards the air. Instead, light with $k_0 < k_{||} < k_{max}$ will be totally reflected and captured by the objective.

Appendix B

OPTICAL DATA

B.1 Optical data

B.1.1 CIGSe

Fig. B.1 shows the real (n) and imaginary (κ) part of the refractive index for each material as function of the wavelength. The data, which was also used in the previous FDTD simulations, was obtained from the ellipsometry measurements from ref. [5]. From the figure we can see that the refractive index of CIGSe ranges from 2.8 to 3.1 in the entire visible range, which is higher than the index for the rest of materials that constitute the solar cell. In a similar fashion, the absorption coefficient (fig. B.1, b), with a peak at around 420 nm and decreasing towards zero at 1200 nm, is higher than any other constituent material, and only CdS has a non-zero absorption at small wavelengths.

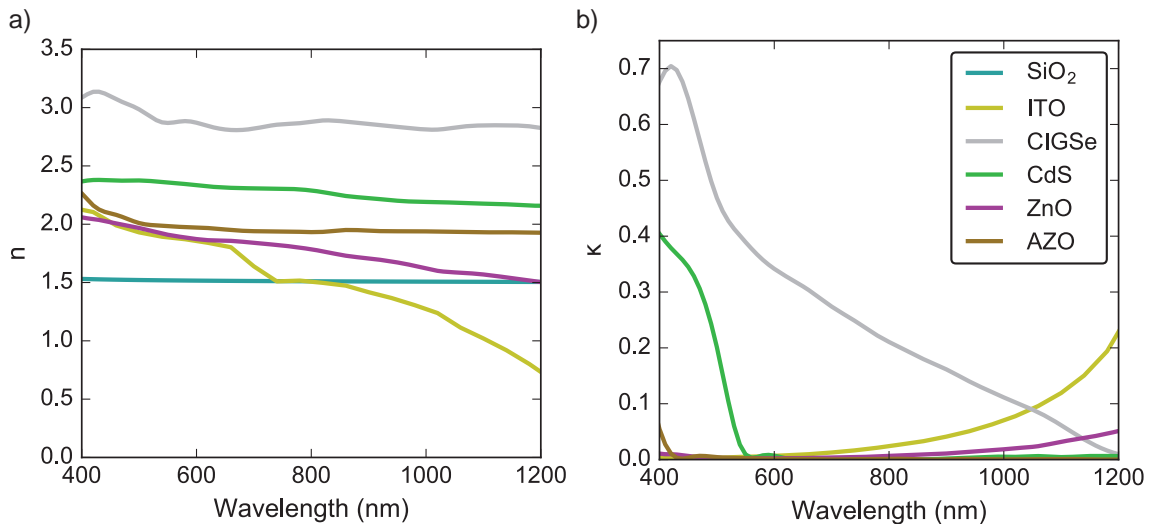


Figure B.1: **Optical data of the constituents materials of a CIGSe solar cell.** (a) Real and (b) imaginary part of the refractive index, obtained from ellipsometry measurements [5]. The refractive index, n , of CIGSe is higher than the one of the adjacent materials in the solar cell geometry for all wavelengths, thus allowing the support of optical waveguide modes. The absorption coefficient, κ , of CIGSe exhibits a peak at wavelength 420 nm and decreases slowly down to zero for $\lambda=1200$ nm. The rest of the materials show an almost zero absorption in the visible range, with only CdS having a significant absorption coefficient between 400 and 500 nm.

B.1.2 CZTS

Obtaining accurate data for the constituent materials of the CZTS cells is crucial for proper light trapping studies. The data for glass, Mo, ZnO and ITO was obtained from ellipsometry measurements. In contrast, fitting the ellipsometry data of CZTS was more difficult and therefore we extracted it from the literature. This difficulty is due to the dependence of the final data on sample fabrication, high surface roughness, inhomogeneous composition

over the entire film and presence of secondary phases, among others [27, 45]. Hence, we obtained the optical data from ref. [27], for a sample with similar geometry and preparation method. In a similar fashion, we considered a buffer layer of CdS instead of $\text{Zn}_{0.35}\text{Cd}_{0.65}\text{S}$ and extracted the refractive index from ref. [4]. Our simulations are based on this optical data, meaning that are convenient to study the general light trapping trends but might deviate from the final behaviour of a real solar cell.

The refractive index of the constituent materials are plotted in fig. B.2, with (a) and (b) being the real (n) and imaginary (κ) part, respectively. We can observe that the refractive index (a) of CZTS ranges from 2.4 to 2.8 in the visible wavelength range and is higher than for the rest of materials, except for a small range of wavelengths around 500 nm, where CdS also exhibits a high index. Therefore, we expect the film of CZTS to support a certain amount of waveguide modes, which is the basis for our approach for light trapping. In addition to this, from the spectrum of the absorption coefficient plotted in (b) we can observe that the one from CZTS has a maximum at around 420 nm and decreases from there on, reaching very small values from 850 nm on. However, it does not reach absolute zero until a wavelength of 1200 nm. In contrast, molybdenum has a much higher absorption coefficient, as expected because of its metal behaviour. In practical terms, this means that a large fraction of the light that is transmitted after the CZTS layer will be absorbed by Mo.

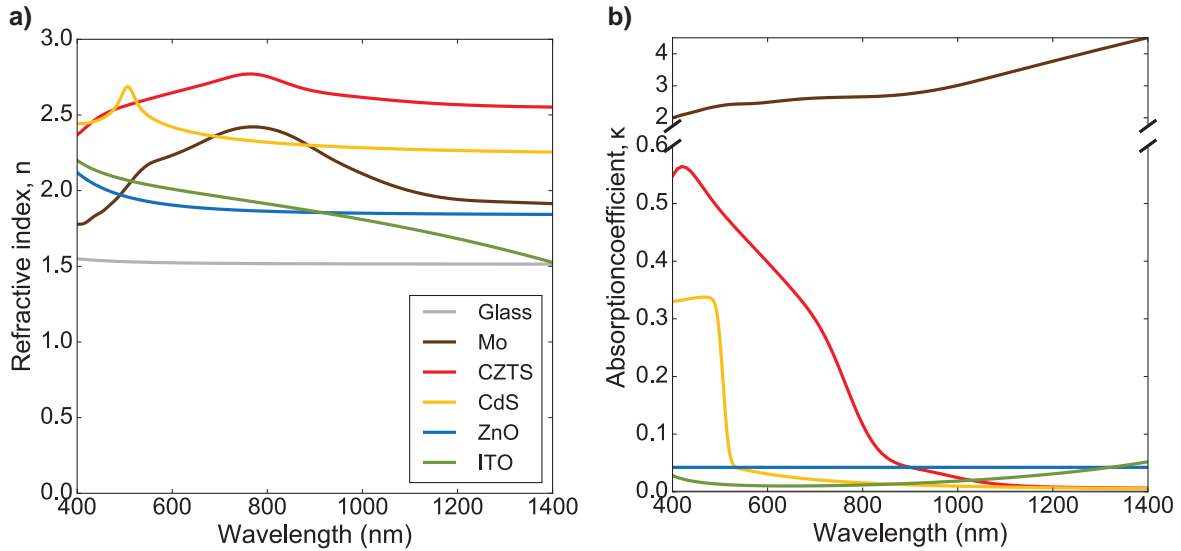


Figure B.2: Optical data of the constituents materials of a CZTS solar cell. (a) Real and (b) imaginary part of the refractive index. The data for glass, Mo, ZnO and ITO was obtained from ellipsometry measurements, while the data for CZTS and CdS were extracted from ref. [27] and [4], respectively. We consider a buffer layer of CdS instead of $\text{Zn}_{0.35}\text{Cd}_{0.65}\text{S}$ due to its easier accessible optical data.

Appendix C

ADDITIONAL INFORMATION OF CL MEASUREMENTS

C.1 Comparison of different regions

Figure C.1 shows the spectra obtained at each of the six different regions that we measured, at short (a) and large (b) wavelengths. The spectra are averaged over the entire area scanned (around $1 \mu\text{m}^2$). The main peak at 920 nm is present in all of the samples, together with a small peak at 520 nm. In the short-wavelength range (a), the sharp peaks are due to errors in the detection and therefore are not related to the CL emission of the sample.

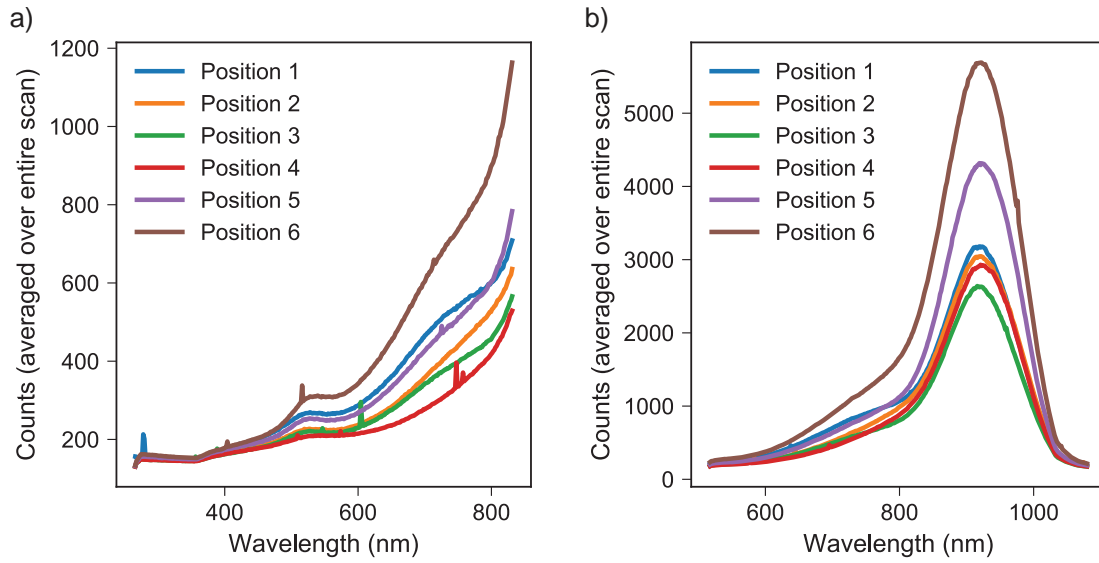


Figure C.1: **CL intensity spectra at different regions.** Spectrum at short (a) and long (b) wavelength. The CL intensity has been averaged over the entire region in each case. We can identify the main spectral features in all cases, which are the peak at 920 nm and the small one at 520 nm.

Following the same procedure, fig. C.2 shows the averaged spectra from seven different regions obtained from low temperature measurements. In this case the main peak is located at around 975 nm and hardly varies in all the regions.

	Gaussian 1	Gaussian 2
Spectrum a	1.34 eV	1.58 eV
Spectrum b	1.33 eV	1.53 eV
Spectrum c	1.33 eV	1.56 eV

Table C.1: **Position of the peaks for the Gaussians used to fit the spectra from fig. C.3.**

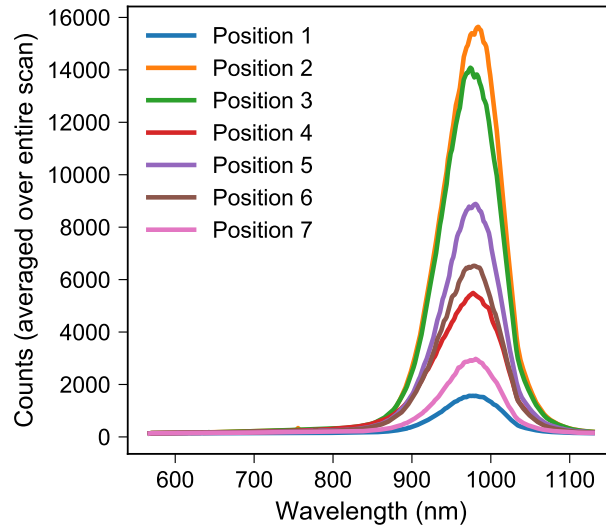


Figure C.2: **CL intensity spectra at different regions for low temperature measurements.** The CL intensity has been averaged over the entire region, each of them with a size around $0.5 \times 0.5 \mu\text{m}^2$. The spectra looks very similar in all cases, with a main peak at 975 nm.

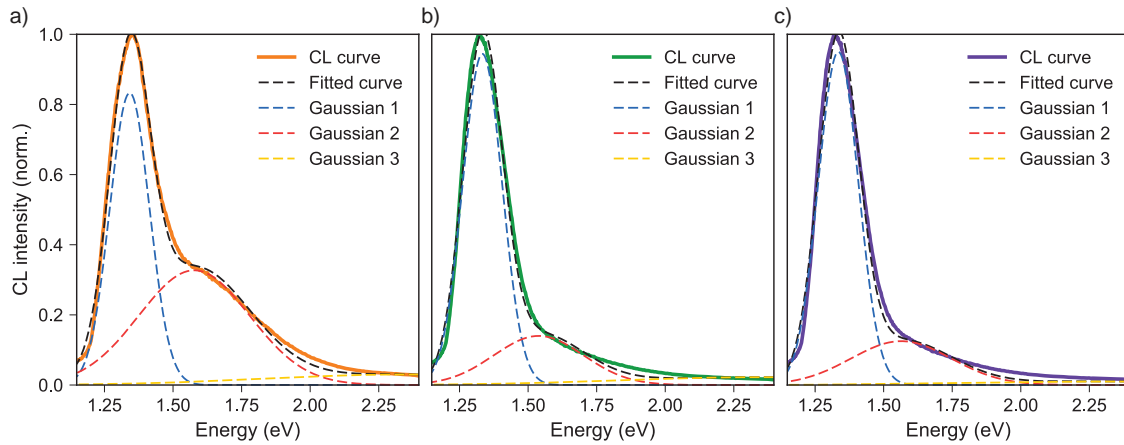


Figure C.3: **Fitted curves for CL spectra at different positions for electron beam energy of 10 keV.** Each plot corresponds to the spectra obtained when the electron beam is placed (a) on top of a CdS particle, (b) on the CdS layer and (c) on the CdS layer with a grain boundary.

C.2 Fitting of the CL spectra

We can fit the CL spectra by considering that each emission process can be described by a Gaussian as a function of energy, and therefore the final spectrum corresponds to the sum of all of them. We have used three Gaussian functions, which would correspond to the emission at wavelengths 520, 760 and 920 nm. Since these spectra are centred around 800 nm, the peak at 520 is practically negligible and thus its contribution is very weak. The fitted curves, together with their sum are shown in C.3 and the position of the two main peaks is summarized in C.1. The strongest peak, fitted with Gaussian 1, is exhibited at 1.33-1.34 eV (932-925 nm), while the second one (Gaussian 2) deviates more among the different spectra, from 1.53 to 1.58 eV (810-784 nm). As a final remark, we should take into account that the efficiency of the spectrometer in dispersing the light is not equal

for all the wavelengths [46], and therefore we have a small uncertainty in the determination of the amount of intensity emitted at each wavelengths, which leads to small differences between the fitted and experimental curves.